Atmos. Meas. Tech., 16, 1971–2000, 2023
https://doi.org/10.5194/amt-16-1971-2023


Atmospheric Measurement Techniques
Open Access
EGU

# The Education and Research 3D Radiative Transfer Toolbox (EaR$^3$T) – towards the mitigation of 3D bias in airborne and spaceborne passive imagery cloud retrievals

**Hong Chen[1,2], K. Sebastian Schmidt[1,2], Steven T. Massie[2], Vikas Nataraja[2], Matthew S. Norgren[2], Jake J. Gristey[3,4], Graham Feingold[4], Robert E. Holz[5], and Hironobu Iwabuchi[6]**

[1]Department of Atmospheric and Oceanic Sciences, University of Colorado, Boulder, CO, USA
[2]Laboratory for Atmospheric and Space Physics, University of Colorado, Boulder, CO, USA
[3]Cooperative Institute for Research in Environmental Sciences, University of Colorado, Boulder, CO, USA
[4]NOAA Chemical Sciences Laboratory, Boulder, CO, USA
[5]Space Science and Engineering Center, University of Wisconsin–Madison, Madison, WI, USA
[6]Center for Atmospheric and Oceanic Studies, Tohoku University, Sendai, Miyagi, Japan

**Correspondence:** Hong Chen (hong.chen-1@colorado.edu)

Received: 2 May 2022 – Discussion started: 29 June 2022
Revised: 15 March 2023 – Accepted: 16 March 2023 – Published: 14 April 2023

**Abstract.** We introduce the Education and Research 3D Radiative Transfer Toolbox (EaR$^3$T, pronounced [ɜːt]) for quantifying and mitigating artifacts in atmospheric radiation science algorithms due to spatially inhomogeneous clouds and surfaces and show the benefits of automated, realistic radiance and irradiance generation along extended satellite orbits, flight tracks from entire aircraft field missions, and synthetic data generation from model data. EaR$^3$T is a modularized Python package that provides high-level interfaces to automate the process of 3D radiative transfer (3D-RT) calculations. After introducing the package, we present initial findings from four applications, which are intended as blueprints to future in-depth scientific studies. The first two applications use EaR$^3$T as a satellite radiance simulator for the NASA Orbiting Carbon Observatory 2 (OCO-2) and Moderate Resolution Imaging Spectroradiometer (MODIS) missions, which generate synthetic satellite observations with 3D-RT on the basis of cloud field properties from imagery-based retrievals and other input data. In the case of inhomogeneous cloud fields, we show that the synthetic radiances are often inconsistent with the original radiance measurements. This lack of radiance consistency points to biases in heritage imagery cloud retrievals due to sub-pixel resolution clouds and 3D-RT effects. They come to light because the simulator's 3D-RT engine replicates processes in nature that conventional 1D-RT retrievals do not capture. We argue that 3D radiance consistency (closure) can serve as a metric for assessing the performance of a cloud retrieval in presence of spatial cloud inhomogeneity even with limited independent validation data. The other two applications show how airborne measured irradiance data can be used to independently validate imagery-derived cloud products via radiative closure in irradiance. This is accomplished by simulating downwelling irradiance from geostationary cloud retrievals of Advanced Himawari Imager (AHI) along all the below-cloud aircraft flight tracks of the Cloud, Aerosol and Monsoon Processes Philippines Experiment (CAMP$^2$Ex, NASA 2019) and comparing the irradiances with the colocated airborne measurements. In contrast to case studies in the past, EaR$^3$T facilitates the use of observations from entire field campaigns for the statistical validation of satellite-derived irradiance. From the CAMP$^2$Ex mission, we find a low bias of 10 % in the satellite-derived cloud transmittance, which we are able to attribute to a combination of the coarse resolution of the geostationary imager and 3D-RT biases. Finally, we apply a recently developed context-aware Convolutional Neural Network (CNN) cloud retrieval framework to high-resolution airborne imagery from CAMP$^2$Ex and show that the retrieved cloud optical thickness fields lead to better 3D radiance consistency than the heritage independent pixel

algorithm, opening the door to future mitigation of 3D-RT cloud retrieval biases.

## 1 Introduction

Three-dimensional cloud effects in imagery-derived cloud properties have long been considered an unavoidable error source when estimating the radiative effect of clouds and aerosols. Consequently, research efforts involving satellite, aircraft, and surface observations in conjunction with modeled clouds and radiative transfer calculations have focused on systematic bias quantification under different atmospheric conditions. Barker and Liu (1995) studied the so-called independent pixel approximation (IPA) bias in cloud optical thickness (COT) retrievals from shortwave cloud reflectance. The bias arises when approximating the radiative transfer relating to COT and measured reflectance at the pixel or cloud column level through one-dimensional (1D) radiative transfer (RT) calculations, while ignoring its radiative context. However, net horizontal photon transport and other effects such as shading engender column-to-column radiative interactions that can only be captured in a three-dimensional (3D) framework, and this can be regarded as a 3D perturbation or bias relative to the 1D-RT (IPA) baseline. The 3D biases not only affect cloud remote sensing but they also propagate into the derived irradiance fields and cloud radiative effects (CREs). Since the derivation of regional and global CREs relies heavily on satellite imagery, any systematic 3D bias impacts the accuracy of the Earth's radiative budget. Likewise, imagery-based aerosol remote sensing in the vicinity of clouds can be biased by net horizontal photon transport (Marshak et al., 2008). Additionally, satellite shortwave spectroscopy retrievals of $CO_2$ mixing ratio are affected by nearby clouds (Massie et al., 2017), albeit through a different physical mechanism than in aerosol and cloud remote sensing.

Given the importance of 3D perturbations for atmospheric remote sensing, ongoing research seeks to mitigate the 3D effects. Cloud tomography, for example, inverts multi-angle radiances to infer the 3D cloud extinction distribution (Levis et al., 2020). This is achieved through iterative adjustments to the cloud field until the calculated radiances match the observations. Convolutional neural networks (CNNs; Masuda et al., 2019; Nataraja et al., 2022) account for 3D radiative transfer (3D-RT) perturbations in COT retrievals through pattern-based machine learning that operates on collections of imagery pixels, rather than treating them in isolation like IPA. Unlike tomography, CNNs require training based on extensive cloud-type-specific synthetic data with the ground truth of cloud optical properties and their associated radiances from 3D-RT calculations. Once the CNNs are trained, they do not require real-time 3D-RT calculations and can therefore be useful in an operational setting. Whatever the future may hold for context-aware multi-pixel or multi-sensor cloud retrievals, there is a paradigm shift on the horizon that started when the radiation concept for the Earth Clouds, Aerosol and Radiation Explorer (EarthCARE; Illingworth et al., 2015) was first proposed (Barker et al., 2012). It foresees a closure loop where broadband radiances, along with irradiance, are calculated in a 3D-RT framework from multi-sensor input fields (Barker et al., 2011) and subsequently compared to independent observations by radiometers pointing in three directions (nadir, forward-, and backward-viewing along the orbit). This built-in radiance closure can serve as an accuracy metric for any downstream radiation products such as heating rates and CREs. Any inconsistencies can be used to nudge the input fields towards the truth in subsequent loop iterations, akin to optimal estimation, or propagated into uncertainties of the cloud and radiation products.

This general approach to radiative closure is also being considered for the National Aeronautics and Space Administration (NASA) Atmospheric Observation System (AOS, developed under the A-CCP, Aerosol and Cloud, Convection and Precipitation study), a mission that is currently in its early implementation stages. Owing to its focus on studying aerosol–cloud–precipitation–radiation interactions at the process level, it requires radiation observables at a finer spatial resolution than achieved with missions to date. At target scales close to 1 km, 3D-RT effects are much more pronounced than at the traditional 20 km scale of NASA radiation products (O'Hirok and Gautier, 2005; Ham et al., 2015; Song et al., 2016; Gristey et al., 2020a). Since this leads to biases beyond the desired accuracy of the radiation products, mitigation of 3D-RT cloud remote sensing biases needs to be actively pursued over the next few years.

Transitioning to an explicit treatment of 3D-RT in operational approaches entails a new generation of code architectures that can be easily configured for various instrument constellations; interlink remote sensing parameters with irradiances, heating rates, and other radiative effects; and used for automated processing of large data quantities. A number of 3D solvers are available for different purposes; for example, the I3RC (International Intercomparison of 3D Radiation Codes; Cahalan et al., 2005) community Monte Carlo code (https://earth.gsfc.nasa.gov/climate/model/i3rc, last access: 26 November 2022), which now also includes an online simulator (http://i3rcsimulator.umbc.edu, last access: 26 November 2022), as described in Várnai et al. (2022) and used in Gatebe et al. (2021); MCARaTS (Monte Carlo Atmospheric Radiative Transfer Simulator, https://sites.google.com/site/mcarats/monte-carlo-atmospheric-radiative-transfer-simulator-mcarats, last access: 26 November 2022; Iwabuchi, 2006); MYSTIC (Monte Carlo code for the physically correct tracing of photons in cloudy atmospheres; Mayer, 2009), which is embedded in libRadtran (library for radiative transfer; Mayer and Kylling, 2005; Emde et al., 2016); McSCIA (Monte Carlo (RT) for SCIAMACHY; Spada et al., 2006), which

is optimized for satellite radiance simulations (including limb-viewing) in a spherical atmosphere; McARTIM (Deutschmann et al., 2011), with several hyperspectral polarimetric applications such as differential optical absorption spectroscopy; and SHDOM (spherical harmonic discrete ordinate method, https://coloradolinux.com/shdom, last access: 26 November 2022; Evans, 1998), which, unlike the other methods, is a deterministic solver with polarimetric capabilities (Doicu et al., 2013; Emde et al., 2015) that is differentiable and can therefore be used for tomography (Loveridge et al., 2022).

For the future operational application of 3D-RT, it is, however, desirable to run various different solvers in one common architecture that automates the processing of various formats of 3D atmospheric input fields (including satellite data), allows the user to choose from various options for atmospheric absorption and scattering, and simulates radiance and irradiance data for real-world scenes. Here, we introduce one such tool that could serve as the seed for this architecture: the Education and Research 3D Radiative Transfer Toolbox (EaR$^3$T, pronounced [ɜːt]). It has been developed over the past few years at the University of Colorado to automate 3D-RT calculations based on imagery or model cloud fields. It can be operated in two ways – (1) with minimal user input, where certain RT parameters are bypassed through default settings, for quick radiation conceptual analysis, and (2) with detailed RT parameters set up by the user for radiation closure purposes. EaR$^3$T is maintained and extended by graduate students as part of their education and applied to various different research projects including machine learning for atmospheric radiation and remote sensing (Gristey et al., 2020b, 2022; Nataraja et al., 2022), as well as radiative closure and satellite simulators. It is implemented as a modularized Python package with various application codes that combine the functionality in different ways, which, once set up, autonomously process large amounts of data required by airborne and satellite remote sensing and for machine learning applications.

The goal of the paper is to introduce EaR$^3$T as a versatile tool for systematically quantifying and mitigating 3D cloud effects in radiation science as foreseen in future missions. To do so, we will first showcase EaR$^3$T as an automated radiance simulator for two satellite instruments, the Orbiting Carbon Observatory-2 (OCO-2, application code 1, App. 1) and the Moderate Resolution Imaging Spectroradiometer (MODIS, application code 2, App. 2) from publicly available satellite retrieval products. In the spirit of radiance closure, the intended use is the comparison of modeled radiances with the original measurements to assess the accuracy of the input data, as follows: operational IPA COT products are made using 1D-RT, and thus the accompanying radiances are consistent with the original measurements under that 1D-RT assumption only. That is, self-consistency is assured if 1D-RT is used in both the inversion and radiance simulation. However, since nature creates 3D-RT radiation fields, we break this traditional symmetry in this paper and introduce the concept of 3D radiance consistency where closure is only achieved if the original measurements are consistent with the 3D-RT (rather than the 1D-RT) simulations. The level of inconsistency is then used as a metric for the magnitude of 3D-RT retrieval artifacts as envisioned by the architects of the EarthCARE radiation concept (Barker et al., 2012).

Subsequently, we discuss applications where EaR$^3$T performs radiative closure in the traditional sense, i.e., between irradiances derived from satellite products and colocated airborne or ground-based observations. The aircraft Cloud, Aerosol and Monsoon Processes Philippines Experiment (CAMP$^2$Ex; Reid et al., 2023), conducted by NASA in the Philippines in 2019, serves as a test bed for this approach. Here, we use EaR$^3$T's automated processing capabilities to derive irradiance from geostationary imagery cloud products and then compare these to cumulative measurements made along all flight legs of the campaign (application code 3, App. 3). In contrast to previous studies that often rely on a number of cases (e.g., Schmidt et al., 2010; Kindel et al., 2010), we perform closure systematically for the entire data set, enabling us to identify 3D-RT biases in a statistically significant manner. Finally, we apply a regional and cloud-type-specific CNN, introduced by Nataraja et al. (2022), that is included with the EaR$^3$T distribution, to high-resolution camera imagery from CAMP$^2$Ex. This last example demonstrates mitigation of 3D-RT biases in cloud retrievals using the concept of radiance closure to quantify its performance against the baseline IPA (application code 4, App. 4).

The general concept of EaR$^3$T, with an overview of the applications and the data used for both parts of the paper is presented in Sect. 2, followed by a description of the procedures of EaR$^3$T in Sect. 3. Results for the OCO-2 and MODIS satellite simulators are shown in Sect. 4, followed by the quantification and mitigation of 3D-RT biases with CAMP$^2$Ex data in Sect. 5 and Sect. 6. A summary and conclusion are provided in Sect. 7.

## 2 Functionality and data flow within EaR$^3$T

### 2.1 Overview

To introduce EaR$^3$T as a satellite radiance simulator tool and to demonstrate its use for the quantification and mitigation of 3D cloud remote sensing biases, five applications (Fig. 1) are included in the GitHub software release.

1. *App. 1* (Sect. 4.1)
   (`examples/01_oco2_rad-sim.py`). The application uses radiance simulations along the track of OCO-2, based on data products from MODIS and other sources, to assess consistency (closure) between simulated and measured radiance.

2. *App. 2* (Sect. 4.2)
   (`examples/02_modis_rad-sim.py`). This application uses MODIS radiance simulations to assess the self-consistency of MODIS level 2 (L2) products with the associated radiance fields (L1B product) under spatially inhomogeneous conditions.

3. *App. 3* (Sect. 5)
   (`examples/03_spns_flux-sim.py`). This application uses irradiance simulations along aircraft flight tracks, utilizing the L2 cloud products of the Advanced Himawari Imager (AHI), and comparisons with aircraft measurements to quantify retrieval biases due to 3D cloud structure based with data from an entire aircraft field campaign.

4. *App. 4* (Sect. 6)
   (`examples/04_cam_nadir_rad-sim.py`). This application uses mitigation of 3D cloud biases in passive imagery COT retrievals from an airborne camera, application of a convolutional neural network (CNN), and subsequent comparison of CNN-derived radiances with the original measurements to illustrate how the radiance self-consistency concept assesses the fidelity of cloud retrievals.

5. *App. 5* (Appendix B)
   (`examples/05_cnn-les_rad-sim.py`). This application uses generation of training data for the CNN (App. 4) based on large eddy simulation (LES) inputs. The training data sets contain (1) the ground truth of COT from the LES data and (2) realistic radiance simulated by EaR$^3$T based on the LES cloud fields.

Figure 1 shows the high-level workflow of the applications. The first four share the general concept of evaluating simulations (the output from the EaR$^3$T, indicated in red at the bottom of each column) with observations (indicated in green at the bottom) from various satellite and aircraft instruments. The workflow of each application consists of three parts – (1) data acquisition, (2) pre-processing, and (3) radiative transfer model (RTM) setup and execution. EaR$^3$T includes functions to ingest data from various different sources, e.g., satellite data from publicly available data archives, which can be combined in different ways to accommodate input data depending on the application specifics. For example, in App. 1, EaR$^3$T is used to automatically download and process MODIS and OCO-2 data files based on the user-specified region, date, and time. Building on the templates provided in the current code distribution, the functionality can be extended to new spaceborne or airborne instruments. Figure 1e shows a fifth application that was developed for earlier papers (Gristey et al., 2020a, b; Nataraja et al., 2022; Gristey et al., 2022). In contrast to the first four, which use imagery products as input, the fifth application ingests model output from a LES and produces irradiance data for surface energy budget applications, or synthetic radiance fields for training a CNN. Details and results are described in the respective papers. The remainder of Sect. 2 introduces the data used in this paper, as well as the input for EaR$^3$T. Subsequently, Sect. 3 describes the EaR$^3$T procedures.

### 2.2 Data

The radiance simulations in App. 1 and App. 2 use data from the OCO-2 and MODIS-Aqua instruments, both of which are in a sun-synchronous polar orbit with an early afternoon Equator crossing time within NASA's A-Train satellite constellation. Figure 2 visualizes radiance measurements by OCO-2 in the context of MODIS Aqua imagery over a partially vegetated and partially cloud-covered land, illustrating that MODIS provides imagery and scene context for OCO-2, which in turn observes radiances from a narrow swath. The region is located in southwestern Colorado in the United States of America. We selected this case because both the surface and clouds are varied along with diverse surface types. The surface features green forest and brown soil, whereas clouds include small cumulus and large cumulonimbus. In addition, this scene contains relatively homogeneous cloud fields in the north and inhomogeneous cloud fields in the south, which allows us to evaluate the simulations from various aspects of cloud morphology. To simulate the radiances of both instruments we use data products from OCO-2 and MODIS, as well as reanalysis products from NASA's Global Modeling and Assimilation Office (GMAO) sampled at OCO-2 footprints and distributed along with OCO-2 data (Sect. 2.2.2).

For App. 3 (irradiance simulations and 3D cloud bias quantification), we use geostationary imagery from the Japanese Space Agency's Advanced Himawari Imager to provide cloud information in the area of the flight path of the NASA CAMP$^2$Ex aircraft (Reid et al., 2023). The AHI data are used in conjunction with aircraft measurements of shortwave spectral radiation (Sect. 2.2.4). Subsequently (App. 4: 3D cloud bias mitigation), we demonstrate the concept of radiance closure under partially cloudy conditions with airborne camera imagery (Sect. 2.2.5). The underlying cloud retrieval is based on a convolutional neural network (CNN), which is described in a related paper (Nataraja et al., 2022) in this special issue and relies on EaR$^3$T-generated synthetic radiance data based on LESs.

#### 2.2.1 Moderate Resolution Imaging Spectroradiometer (MODIS)

The MODIS instruments are multi-use multispectral radiometers onboard NASA's Terra and Aqua satellites, which were launched in 1999 and 2002, respectively. MODIS was conceived as a central element of the Earth Observing System (EOS; King and Platnick, 2018). For App. 1 and App. 2, EaR$^3$T ingests MODIS level 1B radiance products at the

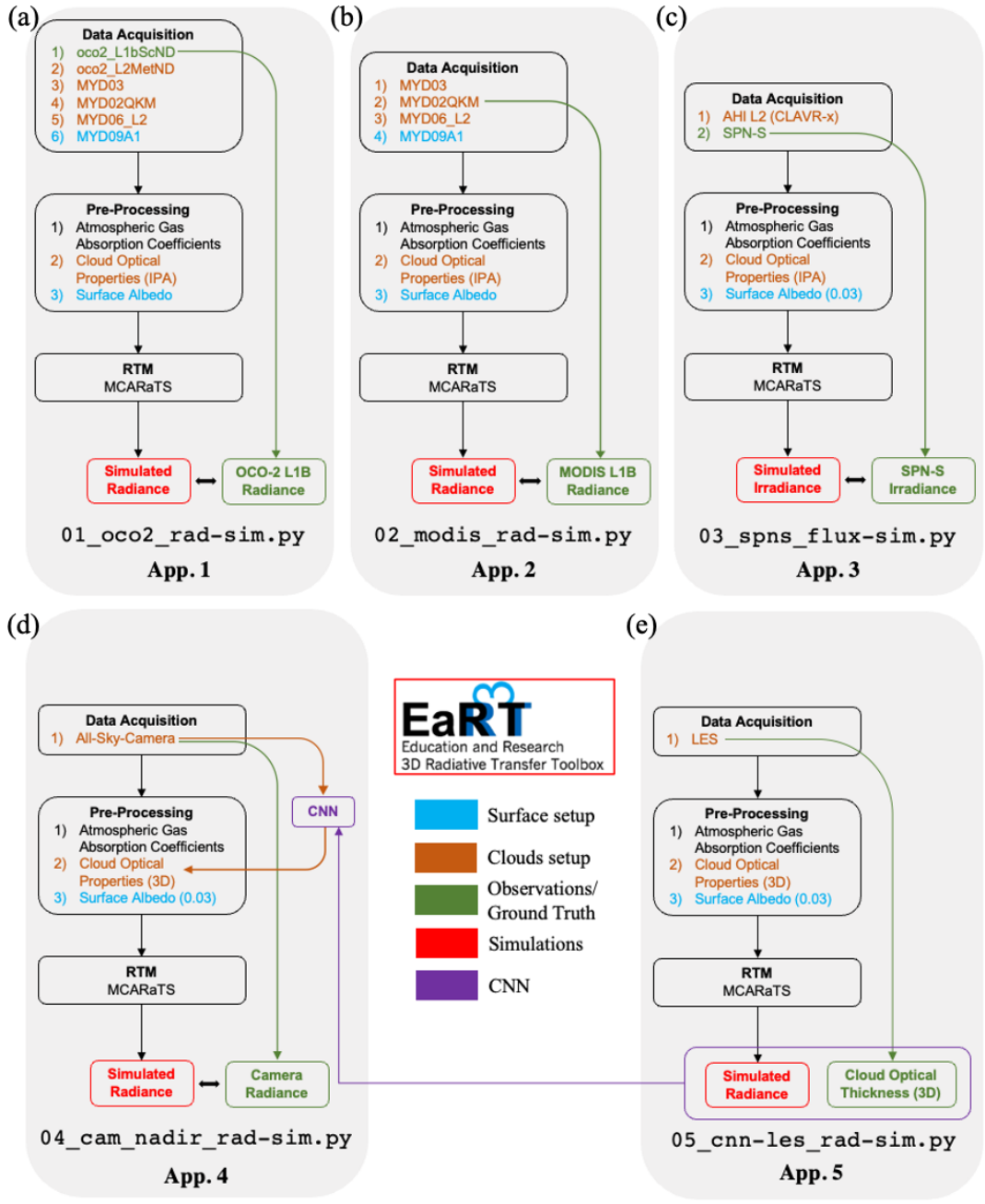


**Figure 1.** Flow charts of EaR$^3$T applications for **(a)** OCO-2 radiance simulation at 768.52 nm (data described in Sect. 2.2.1 and 2.2.2, results discussed in Sect. 4.1), **(b)** MODIS radiance simulation at 650 nm (data described in Sect. 2.2.1, results discussed in Sect. 4.2), **(c)** SPN-S irradiance simulation at 745 nm (data described in Sect. 2.2.3 and 2.2.4, results discussed in Sect. 5), **(d)** all-sky camera radiance simulation at 600 nm (data described in Sect. 2.2.5, results discussed in Sect. 6), and **(e)** radiance simulation at 600 nm based on LES data for CNN training (Appendix B). The data products and their abbreviations are described in Sect. 2.2.

0.25 km scale (channels 1 and 2, bands centered at 650 and 860 nm), MxD02QKM, where "x" stands for "O" in the case of MODIS on Terra, and "Y" in the case of Aqua data), the geolocation product (MxD03), the level 2 cloud product (MxD06), and the surface BRDF (bidirectional reflectance distribution function) product (MCD43A3). For this paper, we mainly use Aqua data (MYD) from data collection 6.1.

For cloud properties in App. 2, we use the MODIS cloud product (MxD06L2, collection 6.1). It provides cloud properties, such as cloud optical thickness (COT), cloud-effective radius (CER), cloud thermodynamic phase, cloud top height

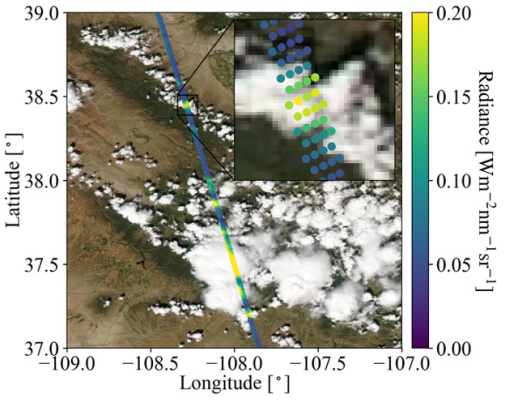


**Figure 2.** OCO-2-measured radiance ($\mathrm{W\,m^{-2}\,nm^{-1}\,sr^{-1}}$) at 768.52 nm, overlaid on MODIS Aqua RGB imagery over southwestern Colorado (USA) on 2 September 2019. The inset shows an enlarged portion along the track, illustrating that OCO-2 radiances co-vary with MODIS-Aqua radiance observations (the circles are used to indicate the geolocation of OCO-2 footprints).

(CTH), etc. (Nakajima and King, 1990; Platnick et al., 2003). Since 3D cloud effects such as horizontal photon transport are most significant at small spatial scales (e.g., Song et al., 2016), we use the high-resolution red (650 nm) channel 1 (250 m) and derive COT directly from the reflectance in the level 1B data (MYD02QKM) instead of using the coarser-scale operational product from MYD06. CER and CTH are sourced from MYD06 and re-gridded to 250 m. The EaR$^3$T strategy for MODIS data is similar, in principle, to the more advanced method by Deneke et al. (2021), which uses a high-resolution wide-band visible channel from geostationary imagery to up-sample narrow-band coarse-resolution channels. However, we simplified cloud detection and COT retrieval (referred to as $\mathrm{COT_{IPA}}$) from reflectance data for the purpose of our paper by using a threshold method (Appendix C1) and an IPA reflectance-to-COT mapping (Appendix C2). In future versions of EaR$^3$T this will be upgraded to more sophisticated algorithms. A simple algorithm (Appendix D1) is used to correct for the parallax shift based on the sensor geometries and cloud heights. The cloud top height data are provided by the MODIS L2 cloud product, and we assume that the cloud base is the same.

For the surface albedo required by the RTM, we used MCD43A3, which provides BRDF calculated from a combination of Aqua and Terra MODIS and MISR (Multi-Angle Imaging Spectroradiometer) clear-sky observations aggregated over a 16 d period (Strahler et al., 1999). This product contains white-sky albedo (WSA, also known as bihemispherical reflectance), which is obtained by integrating the BRDF over all viewing angles (Strahler et al., 1999). The WSA is available on a sinusoidal grid with a spatial resolution of 500 m for MODIS band 2 and includes atmospheric correction for gas and aerosol scattering and absorption. Assuming a Lambertian surface in this first release of EaR$^3$T, we used the WSA (referred to as surface albedo from now on) as surface albedo input to the RTM.

### 2.2.2 Orbiting Carbon Observatory 2 (OCO-2)

The OCO-2 satellite was inserted into NASA's A-Train constellation in 2014 and flies about 6 min ahead of Aqua. OCO-2 provides the column-averaged carbon dioxide ($CO_2$) dry-air mole fraction ($XCO_2$) through passive spectroscopy based on hyperspectral radiance observations in three narrow wavelength regions, the oxygen A-band ($\sim 0.76\,\mu m$), the weak $CO_2$ band ($\sim 1.60\,\mu m$), and the strong $CO_2$ band ($\sim 2.06\,\mu m$). As shown in the inset of Fig. 2, it takes measurements in eight footprints across a narrow swath. Each of the footprints has a size around 1–2 km, and the spectra for the three bands are provided by separate, co-registered spectrometers (Crisp, 2015).

The OCO-2 data products used are (1) level 1B calibrated and geolocated science radiance spectra (L1bScND), (2) standard level 2 geolocated $XCO_2$ retrievals results (L2StdND), and (3) meteorological parameters interpolated from GMAO (L2MetND) at OCO-2 footprint location. Since MODIS on Aqua flies over a scene 6 min after OCO-2, the clouds move with the wind over this time period. We therefore added a wind correction on top of the parallax-corrected cloud fields obtained from MODIS (Sect. 2.2.1). This was done with the 10 m wind speed data from L2MetND (see Appendix D2). For the same scene as shown in Fig. 2, Fig. 3 shows (a) $\mathrm{COT_{IPA}}$, (b) CER, and (c) CTH, all corrected for both parallax and wind effects (these corrections are shown in Fig. A5 in Appendix D2). The parallax and wind corrections are imperfect as certain assumptions are involved. For example, they rely on the cloud top height from the MODIS cloud product. In addition, they process the whole scene with one single sensor viewing the geometry. To minimize artifacts introduced by the assumptions, one can apply the simulation to a smaller region.

The OCO-2 data (L2StdND) themselves only provide sparse surface BRDF (referred to as surface albedo from now on) for the footprints that are clear, while EaR$^3$T requires surface albedo for the whole domain. Therefore, we used MCD43A3 as a starting point. However, since MODIS does not have a channel in the oxygen A-band, MODIS band 2 (860 nm) was used as a proxy for the 760 nm OCO-2 channel as follows: we collocated the OCO-2 retrieved 760 nm surface albedo $\alpha_{OCO}$ within the corresponding 860 nm MODIS MCD43A3 data $\alpha_{MOD}$ as shown in Fig. 4a (same domain as Figs. 2 and 3) and calculated a scaling factor assuming a linear relationship between $\alpha_{OCO}$ and $\alpha_{MOD}$ ($\alpha_{OCO} = c \cdot \alpha_{MOD}$). Figure 4b shows $\alpha_{OCO}$ versus $\alpha_{MOD}$ for all cloud-free OCO-2 footprints. The red line shows a linear regression (derived scale factor $c = 0.867$). Optionally, the OCO-2-scaled, MODIS-derived surface albedo fields can be replaced by the OCO-2 surface albedo products for pixels where they are available. The replacement is done for App. 1. The scaled

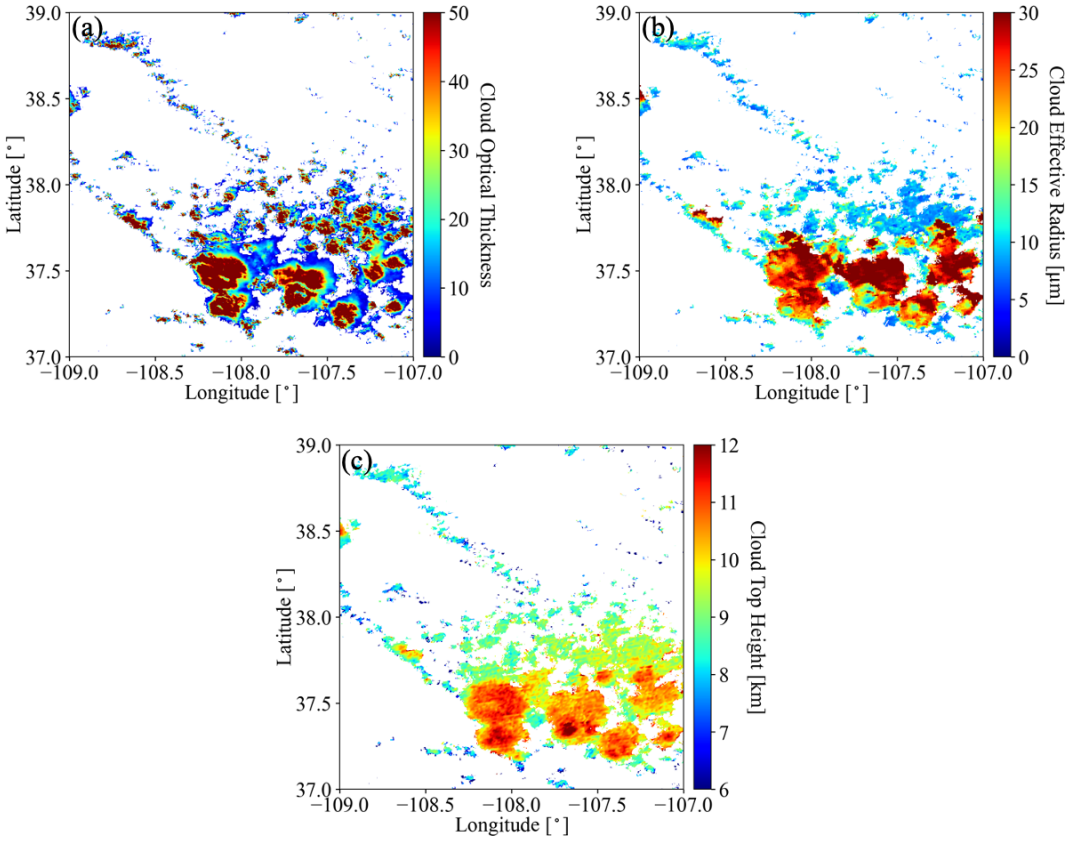


**Figure 3.** **(a)** Cloud optical thickness derived from MODIS L1B radiance at 650 nm by the IPA reflectance-to-COT mapping (Appendix C2), **(b)** cloud effective radius (μm), and **(c)** cloud top height (km) colocated from the MODIS L2 cloud product. The locations of the cloudy pixels were shifted to account for parallax and wind effects. The parallax correction ranged from near zero for low clouds and 1 km for high clouds (10 km CTH). The wind correction was around 0.8 km, given the median wind speed of 2 m s$^{-1}$ to the east.

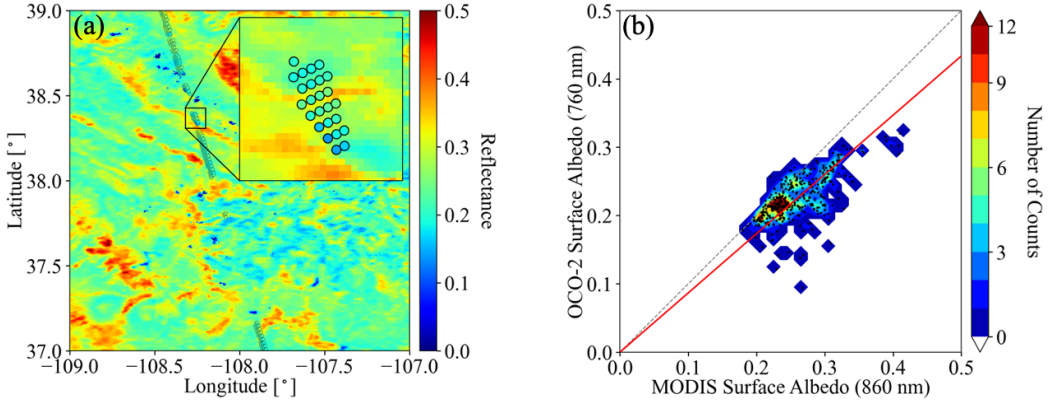


**Figure 4.** **(a)** Surface albedo from the OCO-2 L2 product in the oxygen A-band (near 760 nm), overlaid on the surface albedo from the MODIS MCD43A3 product at 860 nm. **(b)** OCO-2 surface albedo at 760 nm versus MODIS surface albedo at 860 nm, along with linear regression ($\alpha_{OCO} = c \cdot \alpha_{MOD}$) as indicated by the red line (slope $c = 0.867$).

and replaced surface albedo is then treated as input to the RTM assuming a Lambertian surface.

### 2.2.3 Advanced Himawari Imager (AHI)

The Advanced Himawari Imager (AHI, used for App. 3) is a payload on Himawari-8, a geostationary satellite operated by the Meteorological Satellite Center (MSC) of

the Japanese Meteorological Agency. The AHI provides 16 channels of spectral radiance measurements from the shortwave (0.47 µm) to the infrared (13.3 µm). During CAMP$^2$Ex, the NASA in-field operational team closely collaborated with the team from MSC to provide AHI satellite imagery at the highest resolution over the Philippine Sea. From the AHI imagery, the cloud product generation system - Clouds from AVHRR Extended System (CLAVR-x), was used to generate cloud products from the AHI imagery (Heidinger et al., 2014). The cloud products from CLAVR-x include cloud optical thickness, cloud effective radius, and cloud top height at 2 (at nadir) to 5 km spatial resolution. Since AHI provides continuous regional scans every 10 min, the AHI cloud product has a temporal resolution of 10 min.

#### 2.2.4 Spectral Sunshine Pyranometer (SPN-S)

The SPN-S is a prototype spectral version of the commercially available global–diffuse SPN1 pyranometer (Wood et al., 2017; Norgren et al., 2022). The radiometer uses a seven-detector design in combination with a fixed shadow mask that enables the simultaneous measurement of both diffuse and global irradiances, from which the direct component of the global irradiance is calculated via subtraction. The detector measures spectral irradiance from 350 to 1000 nm, and the spectrum is sampled at 1 nm resolution with 1 Hz timing.

During the CAMP$^2$Ex mission, the SPN-S was mounted to the top of the NASA P-3 aircraft, where it sampled downwelling solar irradiance. To ensure accurate measurements, pre- and post-mission laboratory-based calibrations were completed using tungsten "FEL" lamps that are traceable to a National Institute of Standards and Technology standard. Additionally, the direct and global irradiances were corrected for deviations in the SPN-S sensor plane from horizontal that are the result of changes in the aircraft's pitch or roll. This attitude correction applied to the irradiance data is a modified version of the method outlined in Long et al. (2010). However, whereas Long et al. (2010) employ a "box" flight pattern to characterize the sensor offset angles, in this study an aggregation of flight data containing aircraft heading changes under clear-sky conditions are used as a substitute. The estimated uncertainty of the SPN-S system is 6 % to 8 %, with 4 % to 6 % uncertainty stemming from the radiometric lamp calibration process, and up to another 2 % resulting from insufficient knowledge of the sensor cosine response. The stability of the system under operating conditions is 0.5 %. A thorough description of the SPN-S and its calibration and correction procedures is provided in Norgren et al. (2022). In this paper (App. 3) only the global downwelling irradiance sampled by the 745 nm channel is used.

#### 2.2.5 Airborne All-Sky Camera (ASC)

The All-Sky Camera (used for App. 4) is a commercially available camera (ALCOR ALPHEA 6.0CW, https://www.alcor-system.com/common/allSky/docs/ALPHEA_Camera%20ALL%20SKY%20CAMERA_Doc.pdf, last access: 24 April 2022) with fish-eye optics for hemispheric imaging. It has a charge-coupled device (CCD) detector that measures radiances in red, green, and blue channels. Radiometric and geometric calibrations were performed at the Laboratory of Atmospheric and Space Physics at the University of Colorado, Boulder. The three color channels are centered at 493, 555, and 626 nm for blue, green, and red, respectively, with bandwidths of 50–100 nm. Only radiance data from the red channel are used in this paper. The spatial resolution of the ASC depends on the altitude of the aircraft and the viewing zenith angle. Across the hemispheric field of view of the camera, the resolution of the field angle is approximately constant, at about 0.09°. At a flight level of 5 km, this translates to a spatial resolution of 8 m at nadir. However, due to accuracy limitations of the geometric calibration and the navigational data from an inertial navigation system (INS), the nadir geolocation accuracy could only be verified to within ±50 m. During the CAMP$^2$Ex flights, the camera exposure time was set manually to minimize saturation of the detector. The standard image frame rate is 1 Hz. The precision of the camera radiances is on the order of 1 %, and the radiometric accuracy is 6 %–7 %.

## 3 EaR$^3$T procedures

In the previous section, we described the input data for the EaR$^3$T applications. In this section, we will focus on providing the complete workflow (shown in Fig. 1) for the five applications.

After the required data files have been automatically downloaded in the data acquisition step as described in previous section, EaR$^3$T pre-processes them and generates the optical properties of atmospheric gases, clouds, aerosols, and the surface. In Fig. 1, the mapping from input data to these properties is color-coded component-wise (brown for associated cloud property processing if available, blue for associated surface property processing if available, green for associated ground truth property). The EaR$^3$T code base used in this paper (v0.1.1; Chen et al., 2023) only includes MCARaTS as the 3D RT solver, but others are planned for the future. MCARaTS is a radiative transfer solver that uses a Monte Carlo photon-tracing method (Iwabuchi, 2006). It outputs radiation (radiance or irradiance) based on the inputs of radiative properties of surface and atmospheric constituents (e.g., gases, aerosols, clouds) such as single-scattering albedo, scattering phase function, or asymmetry parameter, and solar- and sensor-viewing geometries. The setup of these input properties is implemented in EaR$^3$T's pre-processing steps, which translates atmospheric properties into solver-specific input with minimum user intervention. To achieve this, EaR$^3$T is modular so that it can be extended as new solvers are added. Although the five specific

applications in this paper do not include aerosol layers, the setup of aerosol fields is fully supported and has been used in other applications (e.g., Gristey et al., 2022). After pre-processing, the optical properties are fed into the RT solver. Finally, the user obtains radiation output from EaR$^3$T, i.e., either radiance or irradiance. The output is saved in HDF5 format and can be easily distributed and accessed by various programming languages. The data variables contained in the HDF5 output are provided in Table A2 in Appendix A1.

The processes of data acquisition, pre-processing, and RTM setup and execution (shown in Fig. 1) are automated such that the 3D-RT and 1D-RT calculations can be performed for any region at any date and time using satellite or aircraft data or other data resources such as LES. A detailed code walk-through of App. 1 and 2 is provided in Appendix A2. Since EaR$^3$T is developed as an educational and research 3D-RT tool collection by students, it is a living code base, intended to be updated over time. The master code modules for the five applications as listed in Fig. 1 are included in the EaR$^3$T package under the examples directory. In the current release (v0.1.1), only a limited documentation for the installation and usage, including example code for EaR$^3$T, is provided. More effort will be dedicated toward documentation in the near-future.

In the following sections, we discuss results obtained from EaR$^3$T, starting with those from `examples/01_oco2_rad-sim.py` and `examples/02_modis_rad-sim.py` (Sect. 4), then those from `examples/03_spns_flux-sim.py` (Sect. 5), and concluding with those from `examples/04_cam_nadir_rad-sim.py` (Sect. 6). The usage of the EaR$^3$T package, including the technical input and output parameters and a code walk-through, is provided in Appendix A.

## 4 EaR$^3$T as a 3D satellite radiance simulator

This section demonstrates the automated 3D radiance simulation for satellite instruments by EaR$^3$T for measured OCO-2 and MODIS radiance based on publicly available MODIS retrieval products. The OCO-2 application is an example of radiance consistency between two distinct satellite instruments where the measurements of one (here, OCO-2) are compared with the simulations based on data products from the other (here, MODIS). The MODIS application, on the other hand, is an example of radiance self-consistency. We will show how inconsistencies can be used for detecting cloud and surface property retrieval biases.

### 4.1 OCO-2 (App. 1)

The OCO-2 radiance measurements at 768.52 nm for our sample scene in the context of MODIS imagery are shown in Fig. 2. For that track segment, Fig. 5a shows the simulated radiance and the measurements as a function of latitude. The radiance was averaged over every 0.01° latitude window from 37 to 39° N (the standard deviation within the bin indicated by the shaded color). In clear-sky regions (e.g., around 38.2° N), the 3D simulations (red) are systematically higher than the measurements (black), even though the footprint-level OCO-2 surface albedo retrieval was used to replace and scale the MCD43 surface albedo field as described in Sect. 2.2.2 (Fig. 4). This is probably because, unlike the MCD43 algorithm which relies on multiple overpasses and multiple days for cloud-clearing, the OCO-2 retrieval is done for any clear footprint. Clouds in the vicinity lead to enhanced diffuse illumination that is erroneously attributed to the surface albedo itself. The EaR$^3$T IPA calculations of the clear-sky pixels (blue) essentially reverse the 3D effect and therefore match the observations better. The 3D calculations enhance the reflectance through the very same 3D cloud effects that led to the enhanced surface illumination in the first place. It is possible to correct this effect by downscaling the surface albedo according to the ratio between clear-sky 3D and IPA calculations, but this process is currently not automated.

In the cloudy locations (radiance value greater than $\sim 0.05$), the IPA calculations match the OCO-2 observations on a footprint-by-footprint level (see Fig. 5b), demonstrating that wind and parallax corrections were performed successfully. Of course, there is not always a perfect agreement because of morphological changes in the cloud field over the course of 6 min. It is, however, apparent that the 3D calculations agree to a much lesser extent with the observations than the IPA calculations. Just like the mismatch for the clear-sky pixels indicates a bias in the input surface albedo, the bias here means that the input cloud properties (most importantly COT) are inaccurate. For most of the reflectance peaks, the 3D simulations are too low, which means that the input COT is biased low. This is due to 3D cloud effects on the MODIS-based cloud retrieval. Since they are done with IPA, any net horizontal photon transport is not considered, which leads to an apparent surface brightening as noted above at the expense of the cloud brightness. As a result, the COT from darker clouds is significantly underestimated. This commonly known problem (Barker and Liu, 1995), with several aspects discussed in the subsequent EaR$^3$T applications, can be identified by radiance consistency checks such as the one shown in Fig. 5 and mitigated by novel types of cloud retrievals that do take horizontal photon transport into account (Sect. 6).

### 4.2 MODIS (App. 2)

To go beyond the OCO-2 track and understand the bias between simulated and observed radiances from a domain perspective, we now consider the radiance simulations for the MODIS 650 nm channel. The setup is exactly the same as for the OCO-2 simulations, except that (1) the viewing zenith

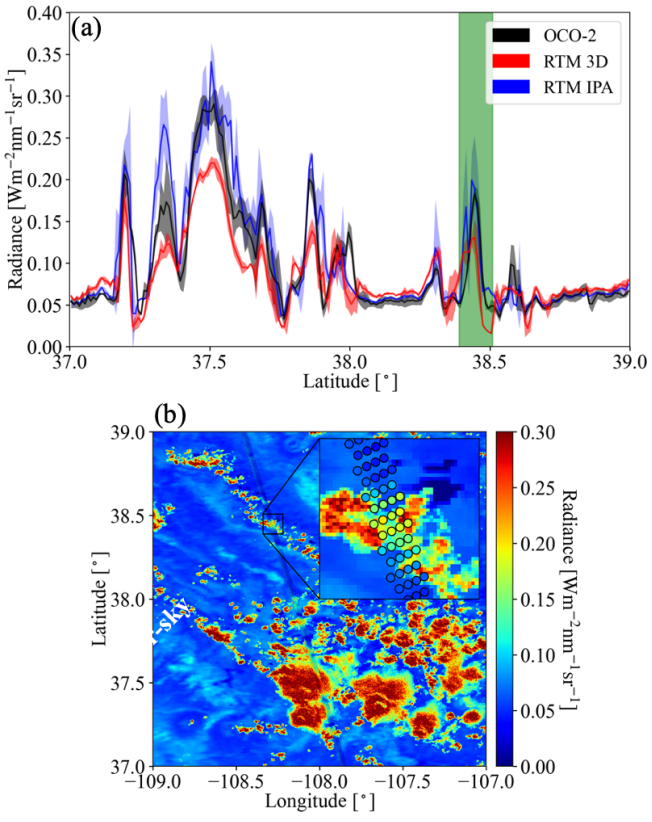


**Figure 5. (a)** Latitudinally averaged (0.01° spacing) radiance calculations from EaR$^3$T (red: 3D; blue: IPA) and OCO-2 measured radiance at 768.52 nm (black) The green shaded area indicates the inset shown in **(b)**. **(b)** The same as Fig. 2 except OCO-2 measured radiance overlaid on IPA radiance simulations at 768.52 nm. The solar zenith angle (SZA) for the radiance simulation case is 34.3°.

angle is set to the average viewing zenith angle of MODIS within the shown domain (instead of OCO-2) and (2) the surface albedo (or WSA) from MCD43 is used directly, this time from the 650 nm channel without rescaling. Figure 6a shows the MODIS-measured radiance field, while Fig. 6b shows the EaR$^3$T 3D simulations. Visually, the clouds from the EaR$^3$T simulation are generally darker than the observed clouds, which is in line with our aforementioned explanation of net horizontal photon transport. They are also blurrier because radiative smoothing (Marshak et al., 1995) propagates into the retrieved COT fields, which are subsequently used as input to EaR$^3$T. The IPA RT calculations agree with the observations for clouds (see Fig. A4a in Appendix C2), which is expected as the IPA calculations and retrievals go through the same RT process, and the darkening and smoothing effects (referred to as 3D effects) are due to horizontal photon transport. To look at the 3D effects more quantitatively, Fig. 7 shows a heatmap plot of simulated radiance versus observed radiance. It shows that the radiance for cloud-covered pixels (labeled "cloudy") from EaR$^3$T are mostly biased low, while good agreement between simulations and observations was achieved for clear-sky radiance (labeled "clear-sky"). The good agreement over clear-sky regions is expected. As mentioned above, we use MCD43 as surface albedo input, which in contrast to the OCO-2 surface albedo product is appropriately cloud-screened and therefore does not have a high reflectance bias. There is, of course, a reflectance enhancement in the vicinity of clouds, but it is captured by the EaR$^3$T calculations. The fact that the calculations agree with the observations even for clear-sky pixels in the vicinity of clouds shows that the concept of radiance consistency works to ensure correct satellite retrievals even in the presence of clouds. It also corroborates our observation from Sect. 4.1 that $\mathrm{COT}_{\mathrm{IPA}}$ is biased low. Since the MODIS reflectance is not self-consistent with respect to 3D RT calculations using $\mathrm{COT}_{\mathrm{IPA}}$ as shown for the cloudy pixels in Fig. 7, we can identify a bias in the cloud properties even without knowing the ground truth of COT. On the other hand, successful closure in radiance (self-consistency) would provide an indication that the input fields including COT are accurate, although it is certainly a weaker metric than direct verification of the retrievals through aircraft–satellite retrieval validation using observations from in situ instruments.

Summarizing the two satellite radiance simulator applications, one can say that EaR$^3$T enables a radiance consistency check for inhomogeneous cloud scenes. We demonstrated that a lack of simulation–observation consistency (MODIS versus OCO-2) and self-consistency (MODIS versus MODIS) can be traced back to biased surface albedo or cloud fields in the simulator input. This can become a diagnostic tool for the quality of retrieval products from future or current missions, even when the ground truth is not known. Although not shown, the errors in the simulated radiance associated with the fixed-SZA (solar zenith angle) assumption (domain average) are negligible. However, the vertical extent of the clouds affects the simulated radiance – the larger the vertical extent, the larger the 3D effects (more horizontal photon transport). Since we assume (1) a cloud geometric thickness of 1 km for clouds with CTH less than 4 km and (2) a cloud base height of 3 km for clouds with CTH greater than 4 km, the simulated radiance at the satellite sensor level is valid for that proxy cloud only. For clouds that are geometrically thicker than the assumed cloud geometrical thickness, the simulated radiance would be even lower due to enhanced horizontal photon transport. Either way, the comparison with the actual radiance measurements will reveal a lack of closure. Additionally, although the clouds introduce the lion's share of the 3D bias that is identified by the radiance consistency check, additional discrepancies can be introduced in different ways. For example, the topography (mountainous region in Colorado) is not considered by MCARaTS (it is considered by MYSTIC, but this solver has not been implemented yet).

For reference, in term of simulation running time, the MODIS simulation (domain size of $[N_x = 846;\ N_y = 846]$) took about 15 min on a Linux workstation with eight CPUs

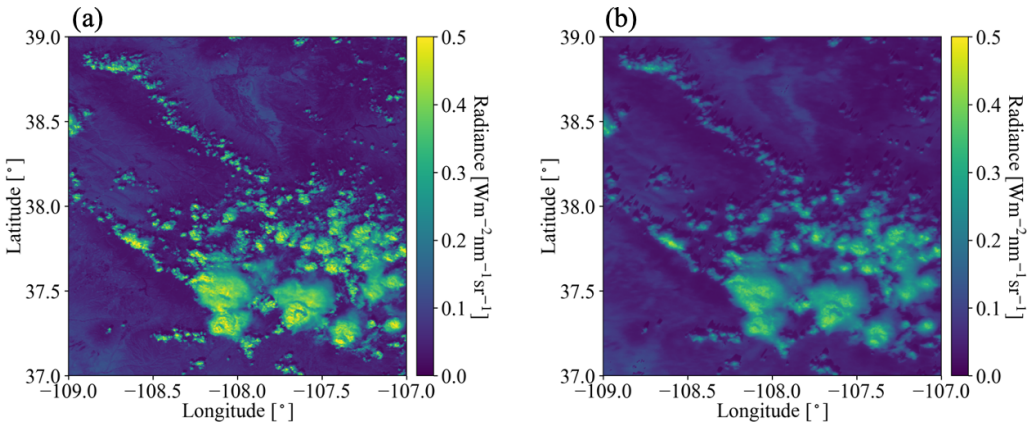


**Figure 6. (a)** MODIS-measured radiance in channel 1 (650 nm). **(b)** Simulated 3D radiance at 650 nm from EaR$^3$T. The solar zenith angle for the radiance simulation case is 34.94°.

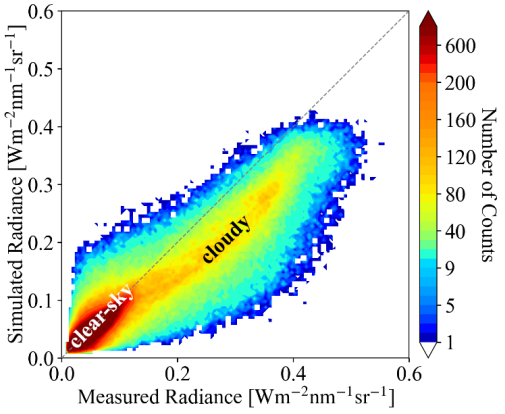


**Figure 7.** Heatmap plot of EaR$^3$T simulated 3D radiance versus MODIS measured radiance at 650 nm.

for three 3D RT runs with $10^8$ photons. With a slightly modified setup and parallelization, the automation can be easily applied for entire satellite orbits, although more research is required to optimize the computation speed depending on the desired output accuracy.

## 5 EaR$^3$T as 3D aircraft irradiance simulator (App. 3)

In contrast to the previous applications that focused on satellite remote sensing, we will now be applying EaR$^3$T to quantify 3D cloud retrieval biases through direct, systematic validation of imagery-derived irradiances against aircraft measurements, instead of using the indirect path of radiance consistency in Sect. 4. Previous studies (e.g., Schmidt et al., 2007; Kindel et al., 2010) conducted radiative closure between remote-sensing-derived and measured irradiance using isolated flight legs as case studies. Here, with the efficiency afforded by the automated nature of EaR$^3$T, we are able to conduct radiative closure of irradiance through a statistical approach that employs campaign-scale amounts of measurement data. Specifically, we used EaR$^3$T to perform large-scale downwelling irradiance simulations at 745 nm based on geostationary cloud retrievals from AHI for the CAMP$^2$Ex campaign, and directly compare these simulations to the SPN-S measured irradiances onboard the P-3 aircraft. This is done for all below-cloud legs from the entire campaign with the aim of assessing the degree to which satellite-derived near-surface irradiances reproduce the true conditions below clouds.

The irradiance simulation process is similar to the previously described radiance simulation in Sect. 4, with only a few modifications. First, we used cloud optical properties from the AHI cloud product (COT, CER, and CTH) as direct inputs into EaR$^3$T. Secondly, we used a constant ocean surface albedo value of 0.03. Such simplification in surface albedo is made under the assumption that (1) the ocean surface is calm with no whitecaps and that (2) the Lambertian BRDF is sufficient (instead of directionally dependent BRDF) to represent surface albedo for the irradiance calculation. Since the ocean surface albedo can greatly differ from 0.03 when the sun is extremely low (Li et al., 2006), we excluded data under low-sun conditions where the SZA is greater than 45°. Lastly, since EaR$^3$T can only perform 3D simulations for a domain at a single specified solar geometry, we divided each CAMP$^2$Ex research flight into small flight track segments where each segment contains 6 min of flight time. The size and shape of the flight track segments can vary significantly due to the aircraft maneuvers, aircraft direction, aircraft speed, etc. For each flight track segment, EaR$^3$T performs irradiance simulations for a domain that extends half a degree at an averaged solar zenith angle. In contrast to the radiance simulation, which has two-dimensional output at a specified altitude and sensor geometry, the irradiance simulation provides three-dimensional output. In addition to $x$ (longitude) and $y$ (latitude) vectors, it has a vertical dimension along $z$ (altitude). From the simulated three-dimensional irra-

diance field, the irradiance for the flight track segment is linearly interpolated to the $x$–$y$–$z$ location (longitude, latitude, and altitude) of the aircraft. EaR$^3$T automatically subdivides the flight track into tiles encompassing track segments and extracts the necessary information from the aircraft navigational data. Based on the aircraft time and position, EaR$^3$T downloads the AHI cloud product that is closest in time and space to the domain containing the flight track segment.

Figure 8 shows the simulated irradiance for a sample flight track below clouds on 20 September 2019. Figure 8a shows the flight track overlaid on AHI imagery. Figure 8b shows 3D (in red) and IPA (in blue) downwelling irradiance simulations for the highlighted flight track in Fig. 8a, as well as measurements by the SPN-S (in black). Since the 3D and IPA simulations are performed separately at discrete solar and sensor geometries for each flight track segment based on potentially changing cloud fields from one geostationary satellite image to the next, discontinuities in the calculations (indicated by dashed gray lines) are expected. The diffuse irradiance (downwelling and upwelling) can also be simulated and compared with radiometer measurements (not shown here). Since the irradiance was simulated and measured below clouds, high values of downwelling irradiance indicate thin-cloud or cloud-free regions, while low values of downwelling irradiance indicate thick-cloud regions. The simulations successfully captured this general behavior – clouds thickened from west to east until around 121.25° E and thinned eastwards. However, the fine-scale variabilities in irradiance were not captured by the simulations due to the coarse resolution of COT in the AHI cloud product (3–5 km). Additionally, the simulations also missed the clear-sky regions in the very east and west of the flight track, as indicated by high downwelling irradiance values measured by SPN-S. This is probably also due to the coarse resolution of the AHI COT product where small cloud gaps are not represented. Large discrepancies between simulations and observations occur in the midsection of the flight track where clouds are present (e.g., longitude range from 121.15 to 121.3°). Although the 3D calculations differ somewhat from the IPA results, they are both biased high, likely because the input COT (the IPA-retrieved AHI product) is biased low. This bias is caused by the same mechanism that was discussed earlier in the MODIS examples (Sect. 4.2). This begs the question as to whether this is true for the entire field mission. To answer the question, we performed a systematic comparison of the cloud transmittance for all available below-cloud flight tracks from CAMP$^2$Ex, using EaR$^3$T's automated processing pipeline. The output of this pipeline is visualized in time-synchronized flight videos (Chen et al., 2022), which show the simulations and observations along all flight legs point by point. These videos give a glimpse of the general cloud environment during the field campaign from the geostationary satellite perspective.

For this comparison, we use transmittance instead of irradiance. The transmittance is calculated by dividing the downwelling irradiance below clouds ($F_{\downarrow}^{\text{bottom}}$) by the downwelling irradiance at the top of the atmosphere extracted from the Kurucz solar spectra ($F_{\downarrow}^{\text{TOA}}$; Kurucz, 1992) at incident SZA, where

$$\text{Transmittance} = \frac{F_{\downarrow}^{\text{bottom}}}{F_{\downarrow}^{\text{TOA}} \cdot \cos(\text{SZA})}. \quad (1)$$

Thus, the transmittance has less diurnal dependence than the irradiance. Figure 9 shows the histograms of the simulated and measured cloud transmittance from all below-cloud legs. The average values are indicated by dashed lines. Although the averaged values of IPA and 3D transmittance are close, their distributions are different. Only the 3D calculations and the measured transmittance reach values beyond 1. This occurs in clear-sky regions in the vicinity of clouds that receive photons scattered by the clouds, as previously discussed for the OCO-2 application.

Both the distribution and the mean value of the simulations are different from the observations. The simulation histograms peak at around 0.9, while the observation histogram peaks at around 1. The histograms indicate that the RT simulations miss most of the clear-sky conditions because of the coarse resolution of the AHI cloud product. If clouds underfill a pixel, AHI interprets the pixel as cloudy in most cases. This leads to an underestimation of clear-sky regions as cumulus and high cirrus were ubiquitous during CAMP$^2$Ex. The area on the left (highlighted in yellow) has low cloud transmittance associated with thick clouds. In this range, the histograms of the calculations are generally below the observations, and the probability density function (PDF) of the calculations is offset to the right (indicated by the yellow arrow). This means that the transmittance is overestimated by both IPA and 3D RT, and thus the COT of thick clouds is underestimated, consistent with what we found before (Fig. 8b). The high-biased transmittance below cloud is also consistent with the findings of low-biased reflectance (App. 1 and 2), both indicating COT of the optically thick clouds are biased low. The high-transmittance end (highlighted in green) is associated with clear-sky and thin clouds. Here, the peak of the PDF is shifted to the left (green arrow), and the calculations are biased low. This is caused by a combination of (1) the overestimation in COT of thin clouds due a 3D bias in the AHI IPA retrieval, (2) the aforementioned resolution effect that underestimates the occurrence of clear-sky regions (or overestimation in cloud fraction), and (3) net horizontal photon transport from clouds into clear-sky pixels. Overall, the calculations underestimate the true transmittance by 10 %. This might seem to contradict Fig. 7, where the calculated reflected radiance was biased low due to the underestimation of COT in the heritage retrievals, which would correspond to an overestimation of the radiation transmitted by clouds. This effect is indeed apparent in the yellow-shaded area of Fig. 9 (high COTs), but the means (dashed lines) show exactly the opposite. To understand that, one has to consider that the histogram depicts all-sky conditions, which include both cloudy

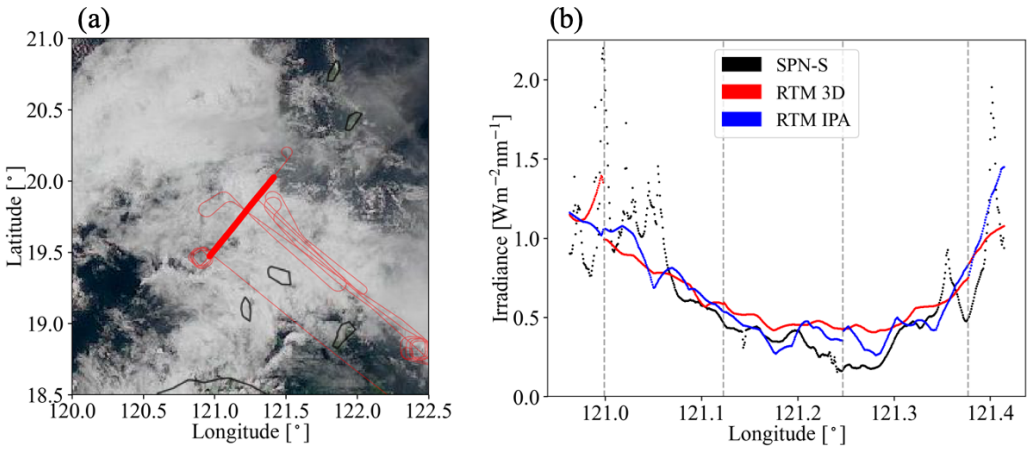


**Figure 8. (a)** Flight track overlay HIMAWARI AHI RGB imagery over the Philippine Sea on 20 September 2019. The thin line shows the entire flight track within the domain. The thick line highlights the specific leg analyzed in **(b)**. **(b)** Measured downwelling irradiance from SPN-S at 745 nm and calculated 3D and IPA irradiance from EaR$^3$T for the highlighted flight track in **(a)**.

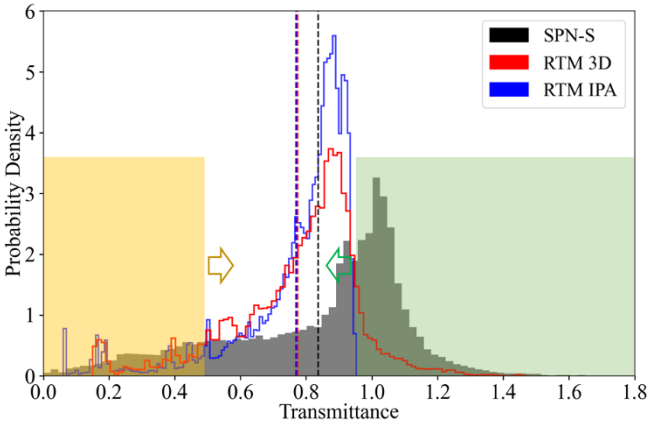


**Figure 9.** Histogram of measured transmittance from SPN-S at 745 nm (dark gray filled area) and calculated 3D (solid red line) and IPA (solid blue line) transmittance from EaR$^3$T for all the below-cloud flight tracks during CAMP$^2$Ex in 2019. The mean values are indicated by dashed lines. The yellow-shaded (green-shaded) area represents the relatively low (high) transmittance region where the probability density of the observed transmittance (dark gray filled area) is greater than the calculations.

and clear pixels. In this case, the direction of the overall (all-sky) bias follows the direction of the thin-cloud or clear bias, rather than the direction of the thick cloud bias. For different study regions of the globe with different cloud fractions, cloud size distributions, and possibly different imager resolutions, the direction and magnitude of the bias might be very different.

Summarizing, this application demonstrates that the EaR$^3$T's automation feature allows systematic simulation-to-observation comparisons. If aircraft observations are available, then closure between satellite-derived irradiance and suborbital measurements is a more powerful verification of satellite cloud retrieval products than the radiance consistency from the earlier standalone satellite applications. Even more powerful is the new approach to process the data from an entire field mission for assessing the quality of cloud products in a region of interest (in this case, the CAMP$^2$Ex area of operation).

## 6 EaR$^3$T for mitigating 3D cloud retrieval biases (App. 4)

In this section, we will use high-resolution imagery from a radiometrically calibrated all-sky camera flown during the CAMP$^2$Ex to isolate the 3D bias (sometimes referred to as IPA bias) and explore its mitigation with a newly developed CNN cloud retrieval framework (Nataraja et al., 2022). The CNN, unlike IPA, takes pixel-to-pixel net horizontal photon transport into account. It exploits the spatial context of pixels in cloud radiance imagery and extracts a higher-dimensional, multi-scale representation of the radiance to retrieve COT fields as the output. It does so by learning on "training data", which in this case was input radiance and COT pairs synthetically generated by EaR$^3$T using LES data from the Sulu Sea. The best CNN model, trained on different coarsened resolutions of the data pairs, is included within the EaR$^3$T repository. For App. 4, this CNN is applied to real imagery data for the first time, which in our case are near-nadir observations by the all-sky camera (Sect. 2.2.5) that flew in CAMP$^2$Ex.

The CNN model was trained at a single (fixed) sun-sensor geometry (SZA of 29.2°, solar azimuth angle (SAA) of 323.8°, and viewing zenith angle (VZA) of 0°) at a spatial resolution of 100 m. We therefore chose a camera scene with a matching SZA (28.9°), rotated the radiance imagery to match SAA of 323.8°, and subsequently gridded the 8–12 m native resolution camera data to 100 m. Figure 10a shows the RGB imagery captured by the all-sky camera over the Philip-

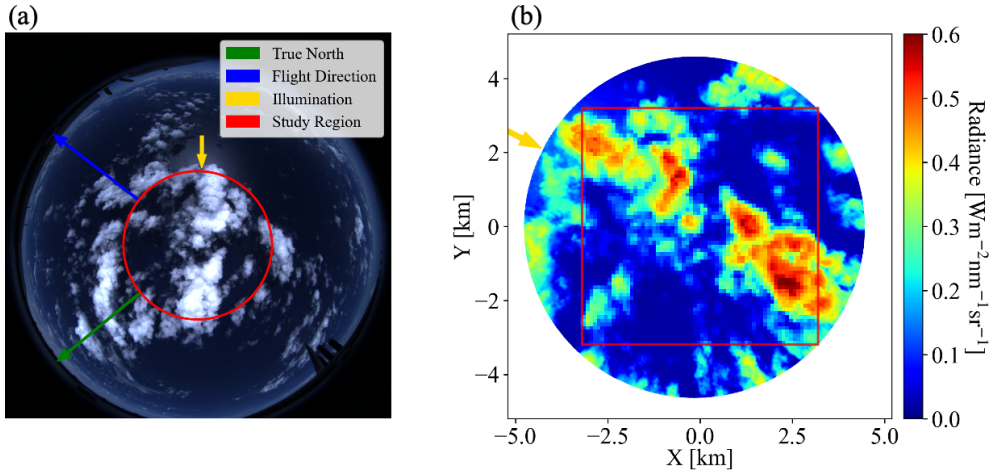


**Figure 10.** **(a)** RGB imagery of nadir-viewing all-sky camera deployed during CAMP$^2$Ex for a cloud scene centered at 15.2744° N, 123.392° E over the Philippine Sea at 02:10:06 UTC on 5 October 2019. The arrows indicate true north (green), flight direction (blue), and illumination (where the sunlight comes from, yellow). **(b)** Red-channel radiance measured by the camera for the circular area indicated by the red circle in **(a)**. The region in the red square shows a gridded radiance with a pixel size of 64 × 64 and spatial resolution of 100 m.

pine Sea at 02:10:06 UTC on 5 October 2019. The sun is located to the southeast (as indicated by the yellow arrow) and can be easily identified from the sun glint. Note that this image has not yet been geolocated; it is depicted as acquired in the aircraft reference frame. Figure 10b shows the rotated scene of the red-channel radiance for the region encircled in yellow in Fig. 10a. The sun (as indicated by the yellow arrow) is now at a SAA of 323.8°. The selected study region is indicated by the red square in Fig. 10b ($6.4 \times 6.4\,\mathrm{km}^2$), where the raw radiance of the camera is gridded at 100 m resolution to match the spatial resolution of the training data set of the CNN.

From the radiance field, we used both the traditional IPA (based on the IPA reflectance-to-COT mapping) and the new CNN to retrieve COT fields. Figure 11 shows the $\mathrm{COT}_{\mathrm{IPA}}$ and $\mathrm{COT}_{\mathrm{CNN}}$ fields, which are visually quite different. For relatively thin clouds (e.g., at around $\{2, 1.8\}$), the CNN tends to retrieve larger COT values than $\mathrm{COT}_{\mathrm{IPA}}$. Also, it returns more spatial structure than the IPA (e.g., around $\{2, -1\}$). To assess how either retrieval performs, we now apply the radiance self-consistency approach introduced with MODIS data in Sect. 4.2. Using both the IPA and the CNN retrieval as input, we had EaR$^3$T calculate the (synthetic) radiance that the camera should have observed if the retrieval were accurate. The clouds are assumed to be located at 1–2 km. Such an assumption is inferred from low-level aircraft observations of clouds on the same day. These radiance fields are shown in Fig. 12a and b and can be compared to Fig. 12c. Seven edge pixels have been removed from the original domain because the CNN performs poorly at edge pixels and because the 3D calculations use periodic boundary conditions.

As evident from the brightest pixels in Fig. 12b and c, the radiances simulated on the basis of the $\mathrm{COT}_{\mathrm{CNN}}$ input are markedly lower than those actually observed by the camera. This is because the CNN was trained on a LES data set with limited COT range that excluded the largest COT that occurred in practice. This means that the observational data went beyond the original training envelope of the CNN, which highlights the importance of choosing the CNN training data carefully for a given region. In Fig. 13, the simulations are directly compared with the original observations, confirming that the CNN-generated data are indeed below the observations on the high radiance end. Otherwise, the CNN-generated radiances agree with the observations. In contrast, the IPA-generated data are biased high for the optically very thin clouds (radiance below 0.1) and systematically biased low for the thick clouds (radiance above 0.2) when compared with the observations, over the dynamic range of the COT, which is indicative of the 3D retrieval bias that we discussed earlier. A small high bias occurs in the $\mathrm{COT}_{\mathrm{CNN}}$-based radiance simulations for the optically thin clouds (radiance value below 0.2). This probably because the CNN training as described by Nataraja et al. (2022) is (1) based on a surface albedo of zero and (2) aerosol-free atmospheric environment (an aerosol-free setup for radiance simulations is also shown in Fig. 13), where in reality the ocean is slightly brighter and atmosphere is mixed with aerosols. Here the radiance self-consistency approach again proves useful despite the absence of ground truth data for the COT. This is valuable because in reality satellite remote sensing does not have the ground truth of COT, whereas radiance measurements are always available. For the CNN, the self-consistency of the radiance is remarkable for most of the clouds (radiance smaller than 0.4), which encompass 86.8 % of the total number of image pixels.

Finally, we use EaR$^3$T to propagate the 3D cloud retrieval bias into the associated bias in estimating the cloud radia-

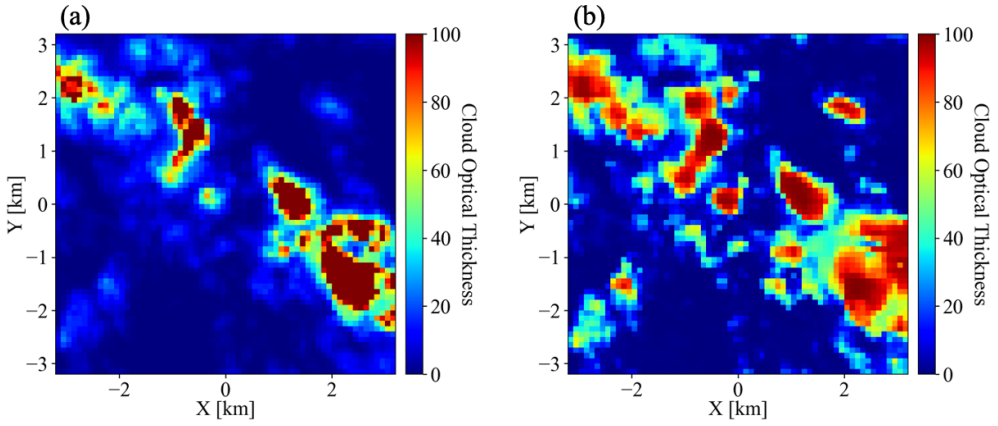


**Figure 11.** Cloud optical thickness for the gridded radiance in Fig. 10b **(a)** estimated by IPA method and **(b)** predicted by CNN.

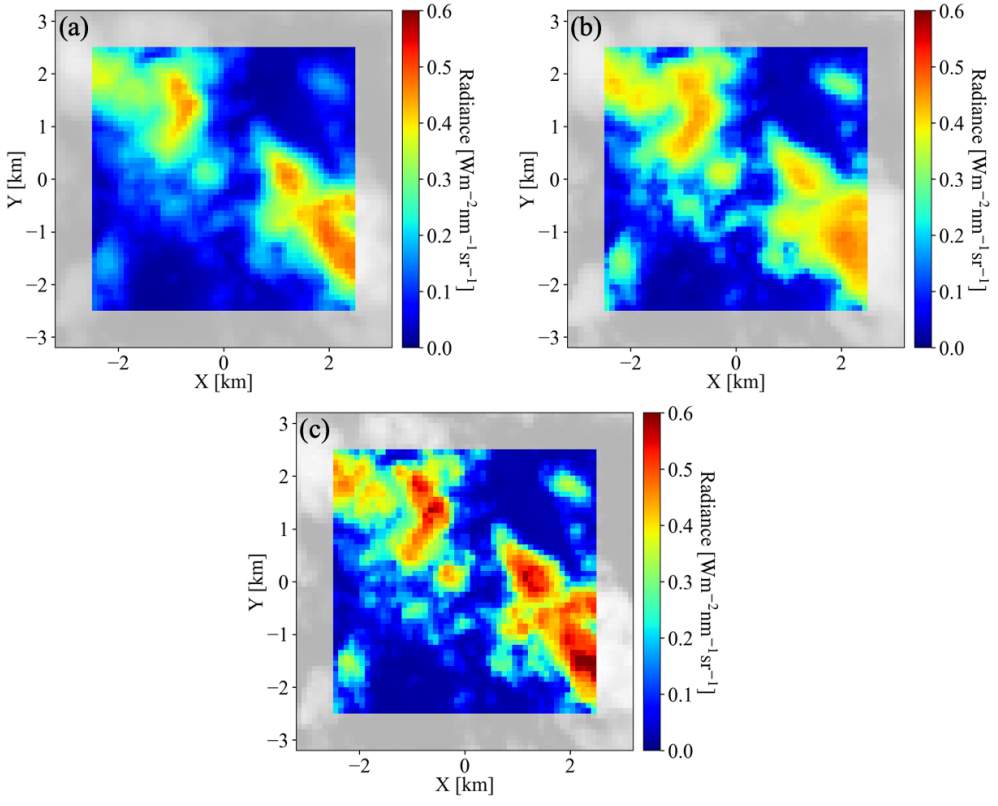


**Figure 12.** The 3D radiance calculations from EaR$^3$T at 600 nm based on cloud optical thickness field **(a)** estimated by IPA and **(b)** predicted by the CNN. The radiance measured by the all-sky camera (the same as Fig. 10b) is provided in the same format in **(c)** for comparison. The calculations were originally performed for the $64 \times 64$ domain. Then seven pixels along each side of the domain (contoured in gray) were excluded, which resulted in a $50 \times 50$ domain.

tive effect from passive imagery retrievals, which means that we are returning from a remote sensing to an energy perspective (irradiance) at the end of the paper. The calculated cloud radiative effects (CRE) of below-cloud (at the surface) and above-cloud (at 2.5 km) regions are shown in Fig. 14a and b, respectively. The most important histograms are those from 3D irradiance calculations based on the CNN retrievals (solid gray line), as this combination would be used in a next-generation framework for deriving CRE from passive remote sensing, and the other important example would be IPA irradiance calculations based on the IPA retrieval (solid red line), as done in the traditional (heritage) approach. The dashed lines are the other combinations. The mean values (red versus gray) indicate that in our case the traditional approach

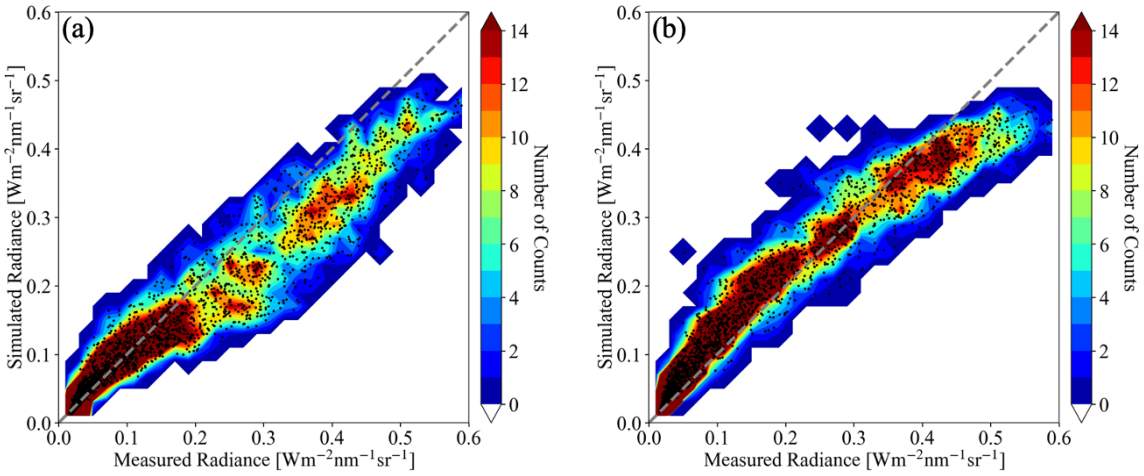


**Figure 13.** Scatter plot superimposed over a 2D histogram of 3D radiance calculations at 600 nm based on cloud optical thickness **(a)** estimated by IPA and **(b)** predicted by the CNN versus measured red-channel radiance from all-sky camera.

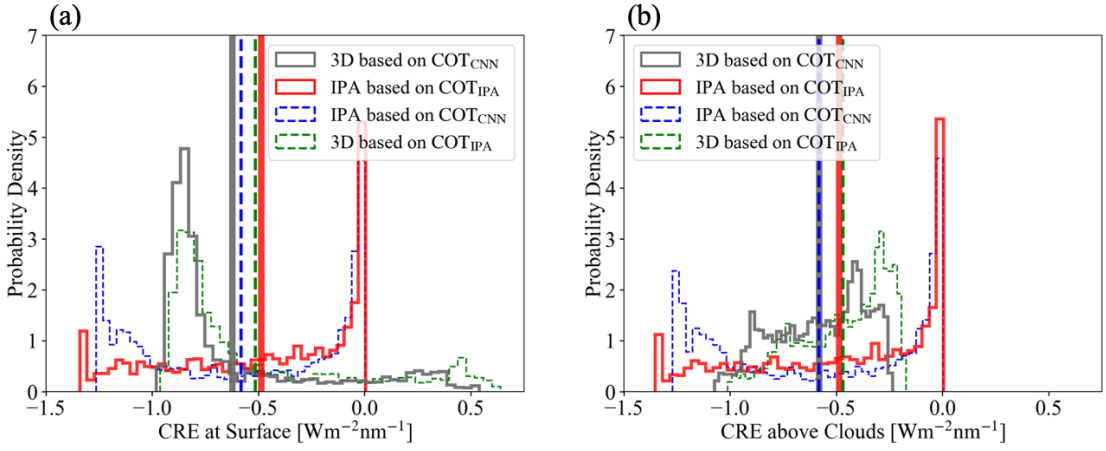


**Figure 14.** Histograms of cloud radiative effects derived from 3D irradiance calculations based on $COT_{CNN}$ (solid gray), IPA irradiance calculations based on $COT_{IPA}$ (solid red), IPA irradiance calculations based on $COT_{CNN}$ (dashed blue), and 3D irradiance calculations based on $COT_{IPA}$ (dashed green) both **(a)** at the surface and **(b)** above the clouds. The mean values are indicated by vertical lines.

would lead to a high bias of more than 28 % at the surface and 20 % above clouds due to low-biased $COT_{IPA}$ (consistent with findings of low-biased $COT_{IPA}$-derived reflectance from Apps. 1 and 2 and high-biased $COT_{IPA}$-derived transmittance from App. 3). Here 3D biases again do not cancel each other out in the domain average. If the CNN had better fidelity even for optically thick clouds, the real bias in CRE would be even larger. A minor but interesting finding is that regardless of which COT retrieval is used, the mean CRE is similar for IPA and 3D irradiance calculations (e.g., $\overline{CRE_{IPA}(COT_{CNN})} \approx \overline{CRE_{3D}(COT_{CNN})}$, vertical dashed blue line locates near the vertical solid gray line) even though the PDFs are different. By far the largest impact on accuracy comes from the retrieval technique, not from the subsequent CRE calculations. Here the self-consistency check again turns out to be a powerful metric to assess retrieval accuracy. Of course, we only used a single case in this part of the paper. For future evaluation of the CNN versus the IPA, one would need to process larger quantities of data in an automated fashion, as was done in the first part of the paper. This is beyond the scope of this introductory paper and will be included in future releases of EaR$^3$T and the CNN.

## 7 Summary and conclusion

In this paper, we introduced EaR$^3$T, a toolbox that provides high-level interfaces to automate and facilitate 1D-RT and 3D-RT calculations. We presented applications that used EaR$^3$T to perform the following tasks:

a. to build a processing pipeline that can automatically simulate 3D radiance fields for satellite instruments (currently OCO-2 and MODIS) from publicly available

satellite surface and cloud products at any given time over any specific region;

b. to build a processing pipeline that can automatically simulate irradiance along all flight legs of aircraft missions, based on geostationary cloud products;

c. to simulate radiance and irradiance for high-resolution COT fields retrieved from an airborne camera using both a traditional 1D-RT (IPA) approach and a newly developed 3D-RT (CNN) approach that considers the spatial context of a pixel.

Unlike other satellite simulators that employ 1D-RT, EaR$^3$T is capable of performing the radiance and irradiance calculations in 3D-RT mode. Optionally, it can be turned off to link back to traditional 1D-RT codes and to calculate 3D perturbations by considering the changes in 3D-RT fields relative to the 1D-RT baseline.

With the processing pipeline referred to in task (a) above (App. 1 and App. 2, Sect. 4), we prototyped a 3D-RT-powered radiance loop (we call it "radiance self-consistency") that is envisioned for upcoming satellite missions such as EarthCARE and AOS. Retrieved cloud fields (in our case, from MODIS and from an airborne camera) are fed back into a 3D-RT simulation engine to calculate at-sensor radiances, which are then compared with the original measurements. Beyond currently included sensors, others can be added easily, taking advantage of the modular design of EaR$^3$T. This radiance closure loop facilitates the evaluation of passive imagery products, especially under spatially inhomogeneous cloud conditions. The automation of EaR$^3$T permits calculations at any time and over any given region, and statistics can be built by looping over entire orbits as necessary. The concept of radiance self-consistency could be valuable even for existing imagery data sets because it allows the automated quantification of 3D-RT biases even without ground truth such as airborne irradiance from suborbital activities. Also, it can be easily extended to spectral or multi-angle observations as available from MODIS and MISR (Multi-Angle Imaging Spectroradiometer), thus providing more powerful constraints to the remote sensing products. In the future it should be possible to include a 3D-RT pipeline such as EaR$^3$T into operational processing of satellite derived data products.

Benefitting from the automation of EaR$^3$T in task (b) above (App. 3, Sect. 5), we performed 3D-RT irradiance calculations for the entire CAMP$^2$Ex field campaign, moving well beyond radiation closure case studies, and instead we systematically evaluated satellite-derived radiation fields with aircraft data for an entire region. From the comparison based on all below-cloud flight tracks during the entire campaign, we found that the satellite-derived cloud transmittance was biased low by 10 % compared to the observations when relying on the heritage satellite cloud product.

From the statistical results of the CAMP$^2$Ex irradiance closure in task (b), we concluded that the bias between satellite-derived irradiances and the ground truth from aircraft measurements was due to a combination of the coarse spatial resolution of the geostationary imagery products and 3D-RT effects. To minimize the coarse-resolution part of the bias and thus to isolate the 3D-RT bias, we used high-resolution airborne camera imagery in task (c) (App. 4, Sect. 6) and found that biases persisted even with increased imager resolution. The at-sensor radiance derived from $\mathrm{COT}_{\mathrm{IPA}}$ was inconsistent with the original measurements. For cloudy pixels, the calculated radiance was well below the observations, confirming an overall low bias in $\mathrm{COT}_{\mathrm{IPA}}$. This low bias could be largely mitigated with the context-aware CNN developed separately in Nataraja et al. (2022) and included in EaR$^3$T. Of course, this novel technique has limitations. For example, the camera reflectance data went beyond the CNN training envelope, which would need to be extended to larger COT values in the future. In addition, the CNN only reproduces two-dimensional cloud fields and does not provide access to the vertical dimension, which will be the next frontier to tackle. Still, the greatly improved radiance consistency from $\mathrm{COT}_{\mathrm{IPA}}$ to $\mathrm{COT}_{\mathrm{CNN}}$ indicates that the EaR$^3$T–LES–CNN approach shows great promise for the mitigation of 3D-RT biases associated with heritage cloud retrievals. We also discovered that for this particular case, the CRE calculated from traditional 1D cloud products can introduce a warm bias of at least 28 % at the surface and 20 % above clouds.

EaR$^3$T has proven to be capable of facilitating 3D-RT calculations for both remote sensing and radiative energy studies. Beyond the applications described in this paper, EaR$^3$T has already been extensively used by a series of ongoing research projects for tasks such as producing massive 3D-RT calculations as training data for a new generation of CNN models (Nataraja et al., 2022), evaluating 3D cloud radiative effects associated with aerosols (Gristey et al., 2022), and creating flight track and satellite track simulations for mission planning. More importantly, the strategies provided in this paper put novel machine learning algorithms on a physical footing, opening the door for the mitigation of complexity-induced biases in the near future. More development effort will be invested into EaR$^3$T in the future, with the goals of minimizing the barriers to using 3D-RT calculations and promoting 3D cloud studies. EaR$^3$T will continue to be an educational tool driven by graduate students. In the future, we plan to add support for additional publicly available 3D RT solvers, e.g., SHDOM (Spherical Harmonic Discrete Ordinate Method; Evans, 1998; Pincus and Evans, 2009), as well as built-in support for HITRAN and associated correlated-$k$ methods (currently, we are implementing such an approach for the longwave wavelength range). From a research perspective, we anticipate that EaR$^3$T will enable the systematic quantification and mitigation of 3D-RT biases of imagery-derived cloud–aerosol radiative effects and may

be the starting point for operational use of 3D-RT for future satellite missions.

## Appendix A

### A1 Technical input and output parameters of EaR$^3$T

EaR$^3$T provides various functions that can be combined to tailored pipelines for automatic 3D radiative transfer (3D-RT) calculations as described in this paper (App. 1–5), as well as for complex research projects beyond. Since EaR$^3$T is written in Python, the modules and functions can be integrated into existing functions developed by the users themselves. Parallelization is enabled in EaR$^3$T by default through multi-processing to accelerate computations. If multiple CPUs are available, EaR$^3$T will distribute jobs for the 3D RT calculations. By default, the maximum number of CPUs will be used. Since EaR$^3$T is designed to make the process of setting up and running 3D-RT calculations simple, some parameters that are unavailable from the input data but are required by the RT solvers are populated via default values and assumptions. However, this does not mean that by using EaR$^3$T one must use these assumptions; they can be easily superseded by user-provided settings. To facilitate this process, Table A1 provides a detailed list of parameters (subject to change in future updates) that can be controlled and modified by the user. In `examples/02_modis_rad-sim.py`, we defined these user-controllable parameters as global variables for providing easy access to the user. In the future, most of the parameters will be controllable through a dedicated configuration file for optimal transparency. These parameters can be changed within the code. For instance, by changing the parameters of "date" (Line 67 in `examples/02_modis_rad-sim.py`) and "region" (Line 68 in `examples/02_modis_rad-sim.py`) within "params" into the following form:

```
params['date'] = datetime.datetime(2022, 2, 10)
params['region'] = [-6.8, -2.8, 17.0, 21.0]
```

one can perform similar RT calculations (as demonstrated in App. 2) for another date and region of interest (here, the western Sahara on 10 February 2022). Note that as the code is under active development, the line numbers are only valid in the version release of v0.1.1 and might change in the future. Given the input parameters, EaR$^3$T will calculate radiance or irradiance and save the calculations into a HDF5 (hierarchical data format version 5) file. The output data variables are provided in Table A2.

In addition to the example code, intuitive and simple examples are provided in `examples/00_er3t_mca.py` and `examples/00_er3t_lrt.py` for users that are interested in learning the basics of setting up EaR$^3$T for calculations. At the current stage, only limited documentation is provided. However, community support is available from the author of this paper through Discord (https://discord.gg/ntqsguwaWv, last access: 6 April 2023). In the near future, more effort will be invested into documentation to give the user more autonomy in creating new applications that cannot be derived from those provided in our paper.

### A2 EaR$^3$T code walk-through

We will provide a code walk-through of the OCO-2 and MODIS simulator applications with the code `examples/01_oco2_rad-sim.py` (App. 1) and `examples/02_modis_rad-sim.py` (App. 2). The data acquisition (first step in Fig. 1) uses functions in `er3t/util`. App. 1 and App. 2 use the functions in `er3t/util/modis.py` and `er3t/util/oco2.py` for downloading the MODIS and OCO-2 data files from the respective NASA data archives and for processing the data (e.g., geo-mapping, gridding). The user supplies minimum input data (date and time, latitudes and longitudes of the region of interest), which need to be specified in `satellite_download` (within the application codes). For example, for App. 1 and App. 2, the only user inputs are the date and time and the region of interest (in this case 2 September of 2019, with the westernmost, easternmost, southernmost, and northernmost longitudes and latitudes being 109° W, 107° W, 37° N, and 39° N, respectively). In order for EaR$^3$T to access any data archives, such as NASA Earthdata, the user needs to create an account with them and store the credentials locally (detailed instructions are provided separately along with the EaR$^3$T distribution).

After the data acquisition step, the satellite data are fed into the pre-processing step for (1) atmospheric gases (`er3t/pre/atm`), (2) clouds (`er3t/pre/cld`), and (3) surface data (`er3t/pre/sfc`), as shown in Fig. 1. In the default configuration of the App. 1, the standard US atmosphere (Anderson et al., 1986; included in the EaR$^3$T repository) is used within `atm.`; EaR$^3$T supports the input of user-specified atmospheric profiles, e.g., atmospheric profiles from reanalysis data for App. 2, by making changes in `atm_atmmod` (from `er3t/pre/atm`). Subsequently, molecular scattering coefficients are calculated by `cal_mol_ext` (from `er3t/util`), and absorption coefficients for atmospheric gases are generated by (`er3t/pre/abs`). At the current development stage, the following two options are available:

1. *Line-by-line* (used by App. 1). The repository includes a sample file of absorption coefficient profiles for a subset of wavelengths within OCO-2's oxygen A-band channel, corresponding to a range of atmospheric transmittance values from low (opaque) to high (so-called "continuum" wavelength). They were generated by an external code based on OCO-2's line-by-line absorption coefficient database (ABSCO; Payne et al., 2020). They are calculated for a fixed mixing ratio of 400 ppm. In a subsequent paper, an OCO-2-specific EaR$^3$T code will

**Table A1.** List of parameters used in the five applications. The line numbers used in the table are referring to the code script of each application. If two line numbers are provided, the first one indicates where the parameter is defined and the second one indicates where the parameter is passed into the radiative transfer setup. Users can change either one for customization purposes. NA: not available.

| Parameters | App. 1 `examples/01_oco2_rad-sim.py` | App. 2 `examples/02_modis_rad-sim.py` | App. 3 `examples/03_spns_flux-sim.py` | App. 4 `examples/04_cam_nadir_rad-sim.py` | App. 5 `examples/05_cnn-les_rad-sim.py` |
|---|---|---|---|---|---|
| Date | 2 September 2019<br>Specified at Line 66: `params['date']`<br>And Line 1569: `date` | 2 September 2019<br>Specified at Line 68: `params['date']`<br>And Line 1311: `date` | 20 September 2019<br>Specified at Line 439: `date`<br>And Line 238: `date` | 5 October 2019<br>Specified at Line 59: `params['date']`<br>And Line 215: `date` | 5 October 2019<br>Specified at Line 58: `params['date']`<br>And Line 126: `date` |
| Geographical region | Specified at Line 69: `params['region']` | Specified at Line 69: `params['region']` | Variable (depends on aircraft location) | NA | NA |
| $Z$ grid (number of grids/ resolution) | 40/0.5 km<br>Specified at Line 1476: `levels` | 40/0.5 km<br>Specified at Line 1220: `levels` | 20/1 km<br>Specified at Line 180: `levels` | 40/0.5 km<br>Specified at Line 174: `levels` | 50/0.4 km<br>Specified at Line 92: `levels` |
| Wavelength | 768.52 nm<br>Specified at Line 67: `params['wavelength']` | 650 nm<br>Specified at Line 67: `params['wavelength']` | 745 nm<br>Specified at Line 440: `wavelength` | 600 nm<br>Specified at Line 58: `params['wavelength']` | 600 nm<br>Specified at Line 57: `params['wavelength']` |
| Atmospheric gas profile | US standard atmosphere<br>Specified at Line 1479: `atm0` | US standard atmosphere<br>Specified at Line 1223: `atm0` | US standard atmosphere<br>Specified at Line 183: `atm0` | US standard atmosphere<br>Specified at Line 177: `atm0` | US standard atmosphere<br>Specified at Line 68: `params['atmospheric_profile']`<br>And Line 94: `atm0` |
| Atmospheric gas absorption | Case specific<br>Specified at Line 1487: `abs0` | Default Absorption Database (Coddington et al., 2008)<br>Specified at Line 1230: `abs0` | Default Absorption Database (Coddington et al., 2008)<br>Specified at Line 189: `abs0` | Default Absorption Database (Coddington et al., 2008)<br>Specified at Line 184: `abs0` | Default Absorption Database (Coddington et al., 2008)<br>Specified at Line 97: `abs0` |
| Cloud top height (CTH) | From MODIS L2 cloud product<br>Specified at Line 1520: `data['cth_2d']`<br>And Line 1530: `cld0` | From MODIS L2 cloud product<br>Specified at Line 1263: `data['cth_2d']`<br>And Line 1273: `cld0` | From AHI L2 cloud product<br>Specified at Line 208: `cth_2d`<br>And Lines 212: `cld0` | 2 km<br>Specified at Line 63: `params['cloud_top_height']`<br>And Lines 199: `cld0` | From LES<br>Specified at Line 103: `cld0` |
| Cloud geometrical thickness | 1 km for CTH < 4 km; Variable that cloud base height is at 3 km for CTH > 4 km<br>Specified at Line 1527: `cgt` | 1 km for CTH < 4 km; Variable that cloud base height is at 3 km for CTH > 4 km<br>And Line 1270: `cgt` | 1 km<br>Specified at Line 212: `cgt` | 1 km<br>Specified at Line 64: `params['cloud_geometrical_thickness']` | From LES<br>Specified at Line 103: `cld0` |
| Cloud optical thickness | Used IPA reflectance-to-COT mapping for MODIS L1B Reflectance at 250 m resolution<br>Specified at Line 1518: `data['cot_2d']`<br>And Line 1530: `cld0` | Used IPA reflectance-to-COT mapping for MODIS L1B Reflectance at 250 m resolution<br>Specified at Line 1261: `data['cot_2d']`<br>And Line 1273: `cld0` | From AHI L2 cloud product<br>Specified at Line 198: `cot_2d`<br>And Lines 212: `cld0` | Used IPA reflectance-to-COT mapping and CNN for camera red channel radiance/reflectance at 100 m resolution<br>Specified at Lines 474 and 493: `cot_2d`<br>And Lines 199: `cld0` | From LES<br>Specified at Line 103: `cld0` |

https://doi.org/10.5194/amt-16-1971-2023

**Table A1.** Continued.

| Parameters | App. 1<br>`examples/01_oco2_rad-sim.py` | App. 2<br>`examples/02_modis_rad-sim.py` | App. 3<br>`examples/03_spns_flux-sim.py` | App. 4<br>`examples/04_cam_nadir_rad-sim.py` | App. 5<br>`examples/05_cnn-les_rad-sim.py` |
|---|---|---|---|---|---|
| Cloud effective radius | From MODIS L2 Cloud Product<br>Specified at Line 1519: `data['cer_2d']`<br>And Line 1530: `cld0` | From MODIS L2 Cloud Product<br>Specified at Line 1262: `data['cer_2d']`<br>And Line 1273: `cld0` | From AHI L2 cloud product<br>Specified at Line 199: `cer_2d`<br>And Lines 212: `cld0` | 12 µm<br>Specified at Lines 475 and 494: `cer_2d`<br>And Lines 199: `cld0` | From LES<br>Specified at Line 103: `cld0` |
| Scattering-phase function | Mie (water cloud)<br>Specified at Line 1536: `pha0`<br>And Line 1573: `sca` | Mie (water cloud)<br>Specified at Line 1279: `pha0`<br>And Line 1315: `sca` | Mie (water cloud)<br>Specified at Line 219: `pha0`<br>And Line 237: `sca` | Mie (water cloud)<br>Specified at Line 190: `pha0`<br>And Line 219: `sca` | Mie (water cloud)<br>Specified at Line 111: `pha0`<br>And Line 130: `sca` |
| Surface albedo | From MODIS surface albedo product and scaled by OCO-2<br>Specified at Line 1501: `mod43`<br>And Line 1503: `sfc_2d` | From MODIS surface albedo product<br>Specified at Line 1244: `mod43`<br>And Line 1246: `sfc_2d` | 0.03<br>Implicitly specified by default at Line 234: `mcarats_ng` | 0.03<br>Specified at Line 61: `params['surface_albedo']`<br>And Line 218: `surface_albedo` | 0.03<br>Specified at Line 59: `params['surface_albedo']`<br>And Line 133: `surface_albedo` |
| Solar zenith angle | From OCO-2 geolocation file<br>Specified at Line 1554: `sza`<br>And Line 1576: `solar_zenith_angle` | From MODIS geolocation file<br>Specified at Line 1296: `sza`<br>And Line 1318: `solar_zenith_angle` | Variable (depends on aircraft location and date and time) | 28.90°<br>Specified at Line 464: `geometry['sza']`<br>And Line 222: `solar_zenith_angle` | 29.16°<br>Specified at Line 60: `params['solar_zenith_angle']`<br>And Line 134: `solar_zenith_angle` |
| Solar azimuth angle | From OCO-2 geolocation file<br>Specified at Line 1555: `saa`<br>And Line 1577: `solar_azimuth_angle` | From MODIS geolocation file<br>Specified at Line 1297: `saa`<br>And Line 1319: `solar_azimuth_angle` | Variable (depends on aircraft location and date and time) | 296.83°<br>Specified at Line 465: `geometry['saa']`<br>And Line 223: `solar_azimuth_angle` | 296.83°<br>Specified at Line 61: `params['solar_azimuth_angle']`<br>And Line 135: `solar_azimuth_angle` |
| Sensor altitude | 705 km (satellite altitude)<br>Implicitly specified by default<br>at Line 1568: `mcarats_ng` | 705 km (satellite altitude)<br>Implicitly specified by default at Line 1310: `mcarats_ng` | NA, three-dimensional irradiance outputs at user-defined $Z$ grid | 5.48 km (flight altitude)<br>Specified at Line 466: `geometry['alt']`<br>And Line 224: `sensor_altitude` | 705 km (satellite altitude)<br>Specified at Line 64: `params['sensor_altitude]`<br>And Line 138: `sensor_altitude` |
| Sensor zenith angle | From OCO-2 geolocation file<br>Specified at Line 1557: `vza`<br>And Line 1578: `sensor_zenith_angle` | From MODIS geolocation file<br>Specified at Line 1302: `vza`<br>And Line 1320: `sensor_zenith_angle` | 0° (nadir)<br>Implicitly specified by default at Line 234: `mcarats_ng` | 0° (nadir)<br>Implicitly specified by default at Line 214: `mcarats_ng` | 0° (nadir)<br>Specified at Line 62: `params['sensor_zenith_angle']`<br>And Line 136: `sensor_zenith_angle` |
| Sensor azimuth angle | From OCO-2 geolocation file<br>Specified at Line 1558: `vaa`<br>And Line 1579: `sensor_azimuth_angle` | From MODIS geolocation file<br>Specified at Line 1303: `vaa`<br>And Line 1321: `sensor_azimuth_angle` | 0° (insignificant for nadir)<br>Implicitly specified by default at Line 234: `mcarats_ng` | 0° (insignificant for nadir)<br>Implicitly specified by default at Line 214: `mcarats_ng` | 0° (insignificant for nadir)<br>Specified at Line 63: `params['sensor_azimuth_angle']`<br>And Line 137: `sensor_azimuth_angle` |

**Table A1.** Continued.

| Parameters | App. 1<br>`examples/01_oco2_rad-sim.py` | App. 2<br>`examples/02_modis_rad-sim.py` | App. 3<br>`examples/03_spns_flux-sim.py` | App. 4<br>`examples/04_cam_nadir_rad-sim.py` | App. 5<br>`examples/05_cnn-les_rad-sim.py` |
|---|---|---|---|---|---|
| Number of photons | $1 \times 10^8$ per run<br>Specified at Line 70: `params['photon']`<br>And Line 1583: `photons` | $1 \times 10^8$ per run<br>Specified at Line 70: `params['photon']`<br>And Line 1325: `photons` | $1 \times 10^7$ per run<br>Specified at Line 50: `params['photon']`<br>And Line 243: `photons` | $1 \times 10^7$ per run<br>Specified at Line 60: `params['photon']`<br>And Line 228: `photons` | $1 \times 10^8$ per run<br>Specified at Line 65: `params['photon']`<br>And Line 141: `photons` |
| Number of runs | 3<br>Specified at Line 1581: `Nrun` | 3<br>Specified at Line 1323: `Nrun` | 3<br>Specified at Line 242: `Nrun` | 3<br>Specified at Line 226: `Nrun` | 3<br>Specified at Line 140: `Nrun` |
| Mode (3D or IPA) | 3D and IPA<br>Specified at Line 1704 and 1705: `solver`<br>And Line 1584: `solver` | 3D or IPA<br>Specified at Line 1418: `solver`<br>And Line 1326: `solver` | 3D and IPA<br>Specified at Lines 377 and 378: `solver`<br>And Line 244: `solver` | 3D<br>Specified at Lines 507 and 508: `solver`<br>And Line 229: `solver` | 3D<br>Specified at Line 143: `solver` |
| Parallelization mode | Python multi-processing<br>Specified at Line 1586: `mp_mode` | Python multi-processing<br>Specified at Line 1328: `mp_mode` | Python multi-processing<br>Specified at Line 247: `mp_mode` | Python multi-processing<br>Specified at Line 231: `mp_mode` | Python multi-processing<br>Specified at Line 145: `mp_mode` |
| Number of CPUs | 12<br>Specified at Line 71: `params['Ncpu']`<br>And Line 1585: `Ncpu` | 12<br>Specified at Line 71: `params['Ncpu']`<br>And Line 1327: `Ncpu` | 12<br>Specified at Line 311: `Ncpu`<br>And Line 246: `Ncpu` | 12<br>Specified at Line 230: `Ncpu` | 24 on clusters<br>Specified at Line 144: `Ncpu` |

**Table A2.** Data variables contained in the output HDF5 file from EaR$^3$T for radiance and irradiance calculations. The radiance is simulated with a user-specified sensor geometry at a given altitude using forward photon tracing. The data variables listed under "metadata" are included for both radiance and irradiance calculations. $N_x$, $N_y$, and $N_z$ are the number of pixels along $x$, $y$, and $z$ direction, respectively. $N_g$ is the number of $g$, as explained in Appendix A2. NA: not available.

| Metadata | | | |
|---|---|---|---|
| Variable name | Description | Data type | Dimension |
| `mean/N_photon` | Number of photons per run | Array | $N_g$ |
| `mean/N_run` | Number of runs | Integer value | NA |
| `mean/toa` | TOA downwelling flux | Float value | NA |
| Radiance | | | |
| Variable name | Description | Data type | Dimension |
| `mean/rad` | Radiance field at user-specified altitude averaged over different runs | Array | $(N_x, N_y)$ |
| `mean/rad_std` | Standard deviation of the radiance fields from different runs | Array | $(N_x, N_y)$ |
| Irradiance | | | |
| Variable name | Description | Data type | Dimension |
| `mean/f_down` | Downwelling irradiance averaged over different runs | Array | $(N_x, N_y, N_z)$ |
| `mean/f_down_std` | Standard deviation of the downwelling irradiance from different runs | Array | $(N_x, N_y, N_z)$ |
| `mean/f_down_diffuse` | Diffuse downwelling irradiance averaged over different runs | Array | $(N_x, N_y, N_z)$ |
| `mean/f_down_diffuse_std` | Standard deviation of the diffuse downwelling irradiance from different runs | Array | $(N_x, N_y, N_z)$ |
| `mean/f_down_direct` | Direct downwelling irradiance averaged over different runs | Array | $(N_x, N_y, N_z)$ |
| `mean/f_down_direct_std` | Standard deviation of the direct downwelling irradiance from different runs | Array | $(N_x, N_y, N_z)$ |
| `mean/f_up` | Upwelling irradiance averaged over different runs | Array | $(N_x, N_y, N_z)$ |
| `mean/f_up_std` | Standard deviation of the upwelling irradiance from different runs | Array | $(N_x, N_y, N_z)$ |

be published where the actual mixing ratio is used. For each OCO-2 spectrometer wavelength within a given channel, hundreds of individual absorption coefficient profiles at the native resolution of ABSCO need to be considered across the instrument line shape (ILS, also known as the slit function) of the spectrometer. The ILS, as well as the incident solar irradiance, is also included in the file. In subsequent steps, EaR$^3$T performs RT calculations at the native spectral resolution of ABSCO, but it then combines the output by convolving with the ILS and outputs OCO-2 radiances or reflectances at the subset of wavelengths. For probabilistic (Monte Carlo) RT solvers such as MCARaTS, the number of photons can be kept relatively low (e.g., $10^6$ photons) and can be adjusted according to the values of the ILS at a particular ABSCO wavelength. Any uncertainty at the ABSCO spectral resolution due to photon noise is greatly reduced by convolving with the ILS for the final output.

2. *Correlated-k* (used by App. 2). This approach (Mlawer et al., 1997) is appropriate for instruments such as MODIS with much coarser spectral resolution than OCO-2 and for broadband calculations. In contrast to the line-by-line approach, RT calculations are not

performed at the native resolution of the absorption database but at Gaussian quadrature points (called "g") that represent the full range of sorted absorption coefficients and then combined using Gaussian quadrature weights. The repository includes an absorption database from Coddington et al. (2008), developed specifically for a radiometer with moderate spectral resolution on the basis of HITRAN (high-resolution transmission molecular absorption database) 2004 (Rothman et al., 2005). It was created for the ILS of the airborne Solar Spectral Flux Radiometer (SSFR, Pilewskie et al., 2003) but is applied to MODIS here, which has a moderate spectral resolution of 8–12 nm with 20–50 nm bandwidth. It uses 16 absorption coefficient bins (g) per target wavelength (this could either be an individual SSFR or a MODIS channel), which are calculated by EaR$^3$T with the Coddington et al. (2008) database using the mixing ratios of atmospheric gases in the previously ingested profile. In future implementations, the code will be updated to enable flexible ILS and broadband calculations.

The `er3t/pre/cld` module calculates extinction, thermodynamic phase, and effective droplet radius of clouds from the input data. The `er3t/pre/pha` module creates the required single-scattering albedo and scattering phase function. The default is a Henyey–Greenstein phase function with a fixed asymmetry parameter of 0.85. Along with the current distribution (v0.1.1) of EaR$^3$T, the Mie scattering phase functions based on thermodynamic phase, effective droplet radius, and wavelength are supported. In this study, App. 1 and App. 2 use Mie scattering phase functions calculated from Legendre polynomial coefficients (originally distributed along with libRadtran) based on the wavelength and cloud droplet effective radius. In the future, EaR$^3$T will include standalone phase functions, which can be chosen on the basis of droplet size distributions in addition to effective radius. It is also possible to include aerosols in a similar fashion to how clouds are included. This is done with the `er3t/pre/aer` module. In the case of aerosols, spectral single-scattering albedo and the asymmetry parameter are required as inputs in addition to the extinction fields.

After the optical properties are calculated, they are passed into the 3D-RT step (`er3t/rtm/mca`). This step performs the setup of RT solver-specified input parameters and data files, distributing runs over multiple CPUs and post-processing RT output files into a single user-friendly HDF5 file. For example, when radiance is specified as output (default in App. 1 and App. 2), key information such as the radiance field and its standard deviation are stored in the final HDF5 file (for details, see Table 1).

While the EaR$^3$T repository comes with the various applications described above, such as App. 1 and App. 2, the functions used by these master or "wrapper" programs can be organized in different ways, where the existing applications serve as templates for a quick start when developing new applications. The functions used by the master code pass information through the various steps as Python objects. For example, in `examples/01_oco2_rad-sim.py`, the downloaded and processed satellite data are stored into the `sat` object. Later, the `sat` object is passed into an EaR$^3$T function to create the `cld` object that contains cloud optical properties. Similarly, EaR$^3$T provides functions to create the `atm` and `sfc` objects with optical properties for atmospheric gases and the surface. These objects (`atm, cld, sfc`) are in turn passed on to solver-specific modules for performing RT calculations. The user can choose to save the data of the intermediate objects into Python pickle files after the first run. In this way, multiple calls with identical inputs can reuse existing data, which accelerates the processing time of EaR$^3$T. Unless the user specifies the `overwrite` keyword argument in the object call to reject saving pickle files, these shortcuts save significant time.

## Appendix B: App. 5 radiance calculations based on the large eddy simulation

The CNN COT retrieval framework was developed by Nataraja et al. (2022). It adapts a U-Net (Ronneberger et al., 2015) architecture and treats the retrieval of COT from radiance as a segmentation problem. Probabilities of 36 COT classes (ranging from COT of 0 to 100) are returned as the final COT retrieved for a given cloud radiance field. This method accounts for horizontal photon transport, which is neglected in traditional cloud retrieval algorithms; in other words, for the spatial context of cloudy pixels. It was trained on synthetic cloud fields generated by a large eddy simulation (LES) model, which provides the ground truth of COT. Subsequently, EaR$^3$T was used to calculate 3D-RT radiances at 600 nm for LES cloud fields to establish a mapping between radiance to COT. Only six LES cases were used to represent the variability of the cloud morphology. Each of these fields are $480 \times 480$ pixels across (spatial resolution of 100 m). These large fields were mapped onto thousands of $64 \times 64$ mini tiles with spatial resolution of 100 m, as described in Nataraja et al. (2022). To keep the training data set small, mini tiles were selectively sampled according to their mean COT and standard deviation. This ensured an even representation of the dynamic range of COT and its variability, which was termed homogenization of the training data set. Figure B1 shows a collection of samples from the training data as an illustration. All the aforementioned simulation setup and techniques in data process are included in the App. 5 example code, which can be applied to the LES data (a different scene from the six scenes) distributed along with EaR$^3$T.

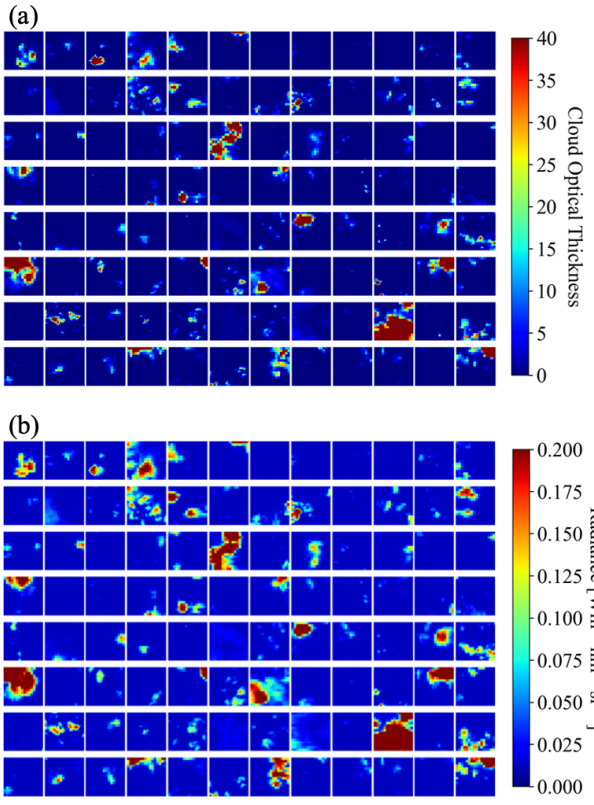


**Figure B1.** Illustrations of $64 \times 64$ tiles of **(a)** cloud optical thickness from LES data and **(b)** calculated 3D radiance at 600 nm from EaR$^3$T for CNN training.

## Appendix C

### C1 Cloud detection and identification

Cloudy pixels are identified through a thresholding method based on the red, green, and blue channels of MODIS. When the radiance values of the red, green, and blue channels of a pixel are all greater than a pre-calculated threshold value, the pixel is considered cloudy, as illustrated by the following equation:

$$\text{If} \quad \begin{array}{l} \text{Red} > a_\text{R} \cdot \text{Quantile}\,(\text{Red}, q_0)\ \& \\ \text{Blue} > a_\text{B} \cdot \text{Quantile}\,(\text{Blue}, q_0)\ \& \\ \text{Green} > a_\text{G} \cdot \text{Quantile}\,(\text{Green}, q_0) \end{array} \left\{ \begin{array}{l} \text{Yes}: \text{cloudy} \\ \text{No}: \text{clear sky} \end{array} \right. , \quad \text{(C1)}$$

where $a_\text{R}$, $a_\text{B}$, and $a_\text{G}$ are scale factors with a default value of 1.0, and quantile returns the $q_0$ percentile of the sorted reflectance data (in ascending order; $q_0 = 0.5$ is equivalent to the median). The scale factors can be adjusted separately to perform fine tuning for different surface types. For example, adjusting $a_\text{G}$ will be more effective for separating clouds from greenish vegetation surface than the other two factors. For simplicity, they are all set to 1.0 for the case shown in App. 1 and 2. The $q_0$ is determined by the following equation:

$$q_0 = \max(0,\ 1 - \text{frac}_\text{cld} \cdot 1.2), \quad \text{(C2)}$$

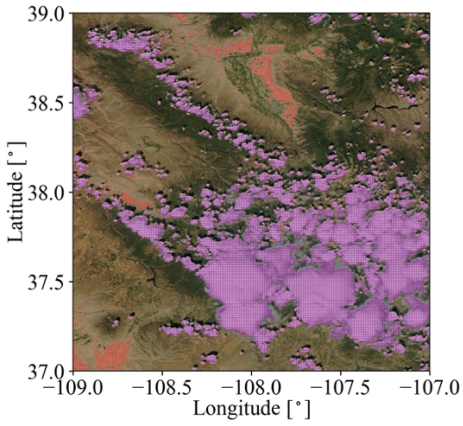


**Figure C1.** Cloud mask for the scene shown in Fig. 2. Red and purple indicate the pixels identified as cloudy through the primary thresholding (Eq. C1), and purple indicates the pixels identified as cloudy after applying the secondary filter (Eq. C3).

where $\text{frac}_\text{cld}$ is cloud fraction obtained from the MODIS L2 cloud product (number of cloudy pixels divided by the number of total pixels). Through the definition of $q_0$, the threshold-based cloud detection method is pegged to the MODIS product at the domain scale. Because of the coarse resolution of the MODIS-based cloud mask, it cannot be used directly for our application. However, it uses many more channels than available at high spatial resolution and is therefore more accurate. The factor of 1.2 can be adjusted. A value of higher than 1 allows for clouds that are not detected by MODIS (for various reasons, for example because of their spatial scale) to be picked up. At the same time, this leads to over-detection (false positives, i.e., clear-sky pixels identified as cloudy), and therefore the thresholding is only the first step (primary thresholding), followed by the next (secondary) step where false positives are removed.

The secondary step is based on MODIS L2 cloud products: COT (cloud optical thickness), CER (cloud effective radius), and CTH (cloud top height). For the pixels that are identified as cloudy in the primary thresholding, especially at the lower end of the reflectance (Ref.), we rely on the clear-sky identifiers from MODIS L2 cloud product (where no cloud products are retrieved), as illustrated by the following equation

$$\text{If} \quad \begin{array}{l} \text{Ref.} < \text{Median}\,(\text{Ref.})\ \& \\ \text{COT, CER, and CTH are NaN} \end{array} \left\{ \begin{array}{l} \text{Yes}: \text{clear sky} \\ \text{No}: \text{cloudy} \end{array} \right. . \quad \text{(C3)}$$

Figure C1 shows the cloud mask from primary thresholding (Eq. C1, red and purple) and the pixels that are reverted to clear sky by the secondary filter (Eq. C2, red).

### C2 IPA reflectance-to-COT mapping

In order to retrieve COT (cloud optical thickness) from cloud reflectance as measured by various instruments, we use the EaR$^3$T built-in solver MCARaTS in IPA mode to calculate a

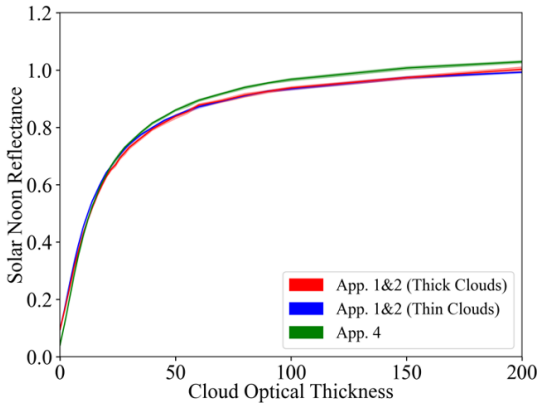


**Figure C2.** The IPA reflectance-to-COT mappings used for Apps. 1 and 2 (red and blue) and App. 4 (green). The reflectance is normalized by the cosine of solar zenith angle (referred to as solar noon reflectance). The uncertainties associated with photon statistics are indicated by the shaded area.

lookup table of reflectance as a function of COT. The function for generating these lookup tables is included in EaR$^3$T as `er3t.rtm.mca.func_ref_vs_cot`. Two mappings are generated for Apps. 1 and 2 to account for geometrically thin (cloud top height less than 4 km) and thick (cloud top height greater than 4 km) clouds separately, while a single mapping is generated for App. 4. Specifically, for a range of COT (0 to 200), reflectance is calculated from EaR$^3$T with the same input parameters (wavelength, viewing and solar geometries, and surface albedo) listed in Table A1 for each application except for a few simplifications described in Table C1.

The clouds are assumed to be horizontally homogeneous over a $2 \times 2$ pixel domain. For each calculation, $10^8$ photons are used for running EaR$^3$T in IPA mode. After calculating $R(\mathrm{COT})$, the inverse relationship of $\mathrm{COT}(R)$ is then used for estimating COT at any given $R$ for the cloudy pixels. Figure C2 shows the IPA reflectance-to-COT mappings created for Apps. 1 and 2 and App. 4. Note that the difference between the Apps. 1 and 2 thin clouds (blue) and App. 4 (green) is due to different surface albedos (when COT is less than 20) and sensor-viewing geometries (when COT greater than 20, specified in Table A1). Note that this approach will ensure IPA radiance and reflectance consistency (retrieved IPA COT will reproduce the exact IPA cloud reflectance; see Fig. C3) because the radiative transfer processes of $R(\mathrm{COT})$ and $\mathrm{COT}(R)$ are the same. However, since it makes some simplifications, as mentioned above, uncertainties are expected for a complicated atmospheric environment (varying cloud thermodynamic phase, effective radius, cloud top height, geometrical thickness, and vertical profile and variable surface albedo and topography), which show up as spread (deviations from identity line) in Fig. C3.

## Appendix D

### D1 Parallax correction

From the satellite's view, the clouds (especially high clouds) will be placed at inaccurate locations on the surface, which have shifted from their actual locations due to the parallax effect. We followed simple trigonometry to correct for it as follows.

Longitude correction (positive from west to east) is performed using the following equation:

$$\delta\mathrm{long} = \frac{(z_{\mathrm{cld}} - z_{\mathrm{sfc}}) \cdot \tan(\theta) \cdot \sin(\phi)}{\pi \cdot R_{\mathrm{Earth}}} \times 180^\circ, \tag{D1}$$

and latitude correction (positive from south to north) is performed using the following equation:

$$\delta\mathrm{lat} = \frac{(z_{\mathrm{cld}} - z_{\mathrm{sfc}}) \cdot \tan(\theta) \cdot \cos(\phi)}{\pi \cdot R_{\mathrm{Earth}}} \times 180^\circ, \tag{D2}$$

where $(\mathrm{long}_{\mathrm{sat}}, \mathrm{lat}_{\mathrm{sat}}, z_{\mathrm{sat}})$ is the satellite location and $\theta$ and $\phi$ (0° at north, positive clockwise) are the sensor-viewing zenith and azimuth angles. $z_{\mathrm{cld}}$ and $z_{\mathrm{sfc}}$ are the cloud top height and the surface height. $R_{\mathrm{Earth}}$ is the radius of the Earth. Figure D1 shows an illustration of the parallax correction for the cloud field in the inset in Fig. 2. Note that discontinuities in the latitude and longitude fields arising from different combinations of sensor-viewing geometries and cloud top and surface heights may lead to gaps in the cloud fields. These gaps are identified and filled in with the average of data from adjacent pixels (plus or minus two pixels along $x$ and $y$) through the following process:

$$\begin{aligned} &\mathrm{If} \quad \mathrm{pixel}_{ij}^{\mathrm{aft}} \text{ is clear \& } \mathrm{pixel}_{ij}^{\mathrm{bef}} \text{ is cloudy \&} \\ &\quad \mathrm{cldfrac}\left(\mathrm{pixel}^{\mathrm{bef}}\left[i-2:i+2,\ j-2:j+2\right]\right) > \mathrm{frac_a} \,\& \\ &\quad \mathrm{cldfrac}\left(\mathrm{pixel}^{\mathrm{aft}}\left[i-2:i+2,\ j-2:j+2\right]\right) > \mathrm{frac_b} \,\& \\ &\begin{cases} \text{Yes}: \text{ fill } \mathrm{pixel}_{ij}^{\mathrm{aft}} \text{ with the average of} \\ \mathrm{cld}(\mathrm{pixel}^{\mathrm{aft}}\left[i-2:i+2,\ j-2:j+2\right]) \end{cases}, \end{aligned} \tag{D3}$$

where $\mathrm{pixel}_{ij}$ indicates the pixel at $i$ along $x$ and $j$ along $y$; bef and aft refer to before and after parallax correction, respectively; cldfrac calculates cloud fraction (number of cloudy pixels divided by total pixel number); and cld selects data where pixels are identified as cloudy. The $\mathrm{frac_a}$ and $\mathrm{frac_b}$ are set to 0.7 for the cases demonstrated in the paper. Lower $\mathrm{frac_a}$ tends to over-select clear-sky pixels at the cloud edge, and lower $\mathrm{frac_b}$ tends to overcorrect clear-sky pixels within clouds that are not clear-sky pixels due to parallax artifacts. Increasing $\mathrm{frac_a}$ and $\mathrm{frac_b}$ values tends to under-correct parallax artifacts.

### D2 Wind correction

The wind correction aims to correct the movement of clouds when advected by the wind between two different satellite overpasses.

**Table C1.** List of parameters for deriving IPA reflectance-to-COT (cloud optical thickness) mappings for Apps. 1 and 2 and App. 4 in addition to those listed in Table A1.

| | App. 1 & 2 | | App. 4 |
|---|---|---|---|
| Cloud type | Geometrically thin clouds | Geometrically thick clouds | All |
| Cloud effective radius | 10 µm | 20 µm | 10 µm |
| Cloud Top Height | 3 km | 10 km | 2 km |
| Cloud geometrical thickness | 1 km | 7 km | 1 km |
| Surface albedo | 0.08 (domain average of the MCD43 WSA) | 0.08 (domain average of the MCD43 WSA) | 0.03 |

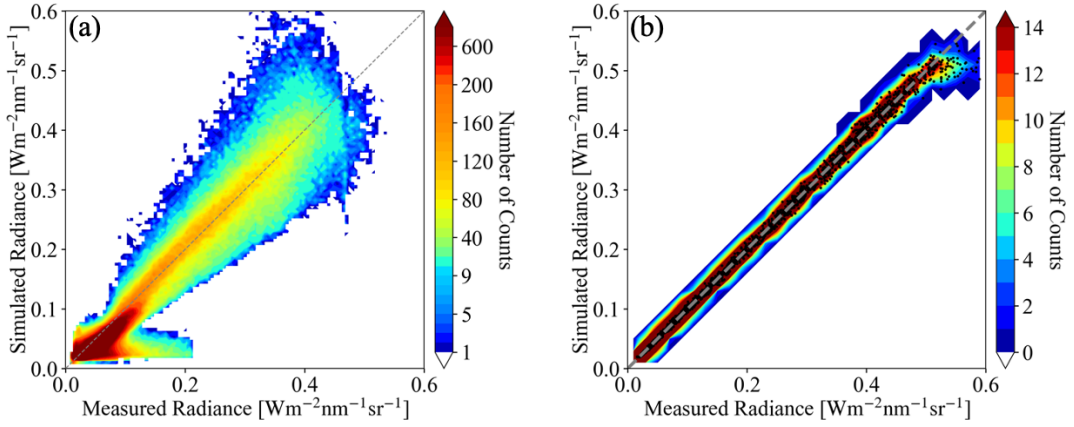


**Figure C3.** Panels **(a)** and **(b)** are the same as Figs. 7 and 13b except for the IPA radiance calculations.

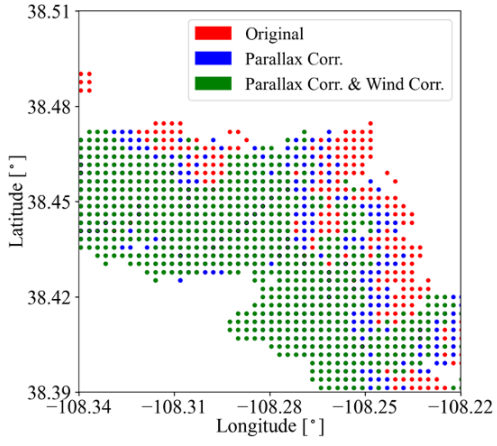


**Figure D1.** An illustration of correcting cloud location (red) for parallax effect (blue) and wind effect (green) for the cloud field of the inset in Fig. 2. Filled cloud gaps are as described in Appendix D1 are indicated by black circles.

Longitude correction (positive from west to east) is performed using the following equation:

$$\delta\text{long} = \frac{\overline{u} \cdot \delta t}{\pi \cdot R_{\text{Earth}}} \times 180^{\circ}, \tag{D4}$$

and latitude correction (positive from south to north) is performed using the following equation:

$$\delta\text{lat} = \frac{\overline{v} \cdot \delta t}{\pi \cdot R_{\text{Earth}}} \times 180^{\circ}, \tag{D5}$$

where $\overline{u}$ and $\overline{v}$ are the domain-averaged 10 m zonal and meridional wind speeds and $\delta t$ is the time difference between two different satellites that fly on the same orbit. Figure D1 shows the cloud location after applying the parallax (Appendix D1) and wind correction for the cloud field in the inset from Fig. 2.

*Code and data availability.* For App. 1 and App. 2, the OCO-2 data were provided by the NASA Goddard Earth Sciences Data and Information Services Center (GES DISC, https://oco2.gesdisc.eosdis.nasa.gov/data, last access: 13 April 2023: https://doi.org/10.5067/6O3GEUK7U2JG, OCO-2 Science Team et al., 2019a; https://doi.org/10.5067/OJZZW0LIGSDH, OCO-2 Science Team et al., 2019b; https://doi.org/10.5067/6SBROTA57TFH, OCO-2 Science Team et al., 2020), and the MODIS data were provided by the NASA Goddard Space Flight Center's level 1 and Atmosphere Archive and Distribution System (LAADS, https://ladsweb.modaps.eosdis.nasa.gov/archive, last access: 13 April 2023: https://doi.org/10.5067/MODIS/MYD03.061, MODIS Characterization Support Team, 2017a; https://doi.org/10.5067/MODIS/MYD02QKM.061, MODIS Characterization Support Team, 2017b; https://doi.org/10.5067/MODIS/MYD06_L2.061, Platnick et al., 2015; https://doi.org/10.5067/MODIS/MCD43A3.061,

Schaaf and Wang, 2021), which are all publicly available and can be downloaded by EaR$^3$T through the application code. For App. 3, the AHI data were processed by Robert E. Holz's (co-author of this paper) team. The SPN-S data were provided by K. Sebastian Schmidt and Matthew S. Norgren (co-authors of this paper). The AHI and SPN-S data are publicly available at NASA Airborne Science Data for Atmospheric Composition (https://www-air.larc.nasa.gov/missions/camp2ex/index.html, last access: 13 April 2023; https://doi.org/10.5067/Suborbital/CAMP2EX2018/DATA001, Reid et al., 2022). The AHI data and the SPN-S data for the flight track indicated in Fig. 8 of the paper are distributed with EaR$^3$T for demonstration purpose. For App. 4, the all-sky camera imagery and CNN model are distributed with EaR$^3$T. EaR$^3$T is publicly available and can be accessed and downloaded at https://github.com/hong-chen/er3t (last access: 6 April 2023; or https://doi.org/10.5281/zenodo.7734965 for v0.1.1 used in this paper; Chen et al., 2023).

*Author contributions.* All of the authors helped with editing the paper. HC developed the EaR$^3$T package in Python including the application code, performed the analysis, and wrote the majority of the paper with input from the other authors. KSS provided an initial MCARaTS simulation wrapper code in Interactive Data Language (IDL), helped with the structure design of EaR$^3$T, and helped with interpreting the results and writing the paper. STM helped with the OCO-2 data interpretation. VN trained and provided the CNN model. MSN helped with the SPN-S instrument calibration and data processing. JJG and GF helped with testing EaR$^3$T and the LES data interpretation. REH provided the AHI data and helped with the data interpretation. HI helped with the implementation of MCARaTS in EaR$^3$T.

*Competing interests.* At least one of the (co-)authors is a member of the editorial board of *Atmospheric Measurement Techniques*. The peer-review process was guided by an independent editor, and the authors also have no other competing interests to declare.

*Disclaimer.* Publisher's note: Copernicus Publications remains neutral with regard to jurisdictional claims in published maps and institutional affiliations.

*Special issue statement.* This article is part of the special issue "Cloud, Aerosol and Monsoon Processes Philippines Experiment (CAMP2Ex) (ACP/AMT inter-journal SI)". It is not associated with a conference.

*Acknowledgements.* The aircraft all-sky camera was radiometrically calibrated by the U.S. Naval Research Laboratory. We thank Jens Redemann for insightful discussions in reference to Fig. 9 (App. 3) about the apparent contradiction regarding the direction of the COT, reflectance, and transmittance biases.

*Financial support.* This research has been supported by the National Aeronautics and Space Administration (grant no. 80NSSC18K0146).

*Review statement.* This paper was edited by Jing Wei and reviewed by Hartwig Deneke, Jana Mendrok, and one anonymous referee.

## References

Anderson, G. P., Clough, S. A., Kneizys, F. X., Chetwynd, J. H., and Shettle, E. P.: AFGL atmospheric constituent profiles (0–120 km), Tech. Rep. AFGL-TR-86–0110, Air Force Geophys. Lab., Hanscom Air Force Base, Bedford, Massachusetts, USA, 1986.

Barker, H. and Liu, D.: Inferring optical depth of broken clouds from Landsat data, J. Climate, 8, 2620–2630, 1995.

Barker, H. W., Jerg, M. P., Wehr, T., Kato, S., Donovan, D. P., and Hogan, R. J.: A 3D cloud construction algorithm for the EarthCARE satellite mission, Q. J. Roy. Meteor. Soc., 137, 1042–1058, https://doi.org/10.1002/qj.824, 2011.

Barker, H. W., Kato, S., and Wehr, T.: Computation of solar radiative fluxes by 1-D and 3-D methods using cloudy atmospheres inferred from A-train satellite data, Surv. Geophys., 33, 657–676, 2012.

Cahalan, R., Oreopoulos, L., Marshak, A., Evans, F., Davis, A., Pincus, R., Yetzen, K. H., Mayer, B., Yetzer, K. H., Mayer, B., Davies, R., Ackerman, T. P., Barker, H. W., Clothiaux, E. E., Ellingson, R. G., Garay, M. J., Kassianov, E., Kinne, S., Macke, A., O'Hirok, W., Partain, P. T., Prigarin, S. M., Rublev, A. N., Stephens, G. L., Szczap, F., Takara, E. E., Varnai, T., Wen, G., and Zhuravleva, T.: The I3RC: Bringing Together the Most Advanced Radiative Transfer Tools for Cloudy Atmospheres, B. Am. Meteorol. Soc., 86, 1275–1293, 2005.

Chen, H., Schmidt, S., and Holz, R. E.: Synchronized Flight Videos for NASA CAMP$^2$Ex, Zenodo [data set], https://doi.org/10.5281/zenodo.7358509, 2022.

Chen, H., Schmidt, S., and Nataraja, V.: hong-chen/er3t: er3t-v0.1.1 (v0.1.1), Zenodo [code], https://doi.org/10.5281/zenodo.7734965, 2023.

Coddington, O., Schmidt, K. S., Pilewskie, P., Gore, W. J., Bergstrom, R., Roman, M., Redemann, J., Russell, P. B., Liu, J., and Schaaf, C. C.: Aircraft measurements of spectral surface albedo and its consistency with ground-based and space-borne observations, J. Geophys. Res., 113, D17209, https://doi.org/10.1029/2008JD010089, 2008.

Crisp, D.: Measuring Atmospheric Carbon Dioxide from Space with the Orbiting Carbon Observatory-2 (OCO-2), P. Soc. Photo.-Opt. Ins., 9607, 960702, https://doi.org/10.1117/12.2187291, 2015.

Deneke, H., Barrientos-Velasco, C., Bley, S., Hünerbein, A., Lenk, S., Macke, A., Meirink, J. F., Schroedter-Homscheidt, M., Senf, F., Wang, P., Werner, F., and Witthuhn, J.: Increasing the spatial resolution of cloud property retrievals from Meteosat SEVIRI by use of its high-resolution visible channel: implementation and examples, Atmos. Meas. Tech., 14, 5107–5126, https://doi.org/10.5194/amt-14-5107-2021, 2021.

Deutschmann, T., Beirle, S., Friess, U., Grzegorski, M., Kern, C., Kritten, L., Platt, U., Prados-Roman, C., Pukite, J., Wagner, T., Werner, B., and Pfeilsticker, K.: The Monte Carlo atmospheric radiative transfer model McArtim: introduction and validation of Jacobians and 3-D features, J. Quant. Spectrosc. Ra., 112, 1119–1137, https://doi.org/10.1016/j.jqsrt.2010.12.009, 2011.

Doicu, A., Efremenko, D., and Trautmann, T.: A multi-dimensional vector spherical harmonics discrete ordinate method for atmospheric radiative transfer, J. Quant. Spectrosc. Ra., 118, 121–131, https://doi.org/10.1016/j.jqsrt.2012.12.009, 2013.

Emde, C., Barlakas, V., Cornet, C., Evans, F., Korkin, S., Ota, Y., Labonnote, L. C., Lyapustin, A., Macke, A., Mayer, B., and Wendisch, M.: IPRT polarized radiative transfer model intercomparison project – Phase A, J. Quant. Spectrosc. Ra., 164, 8–36, https://doi.org/10.1016/j.jqsrt.2015.05.007, 2015.

Emde, C., Buras-Schnell, R., Kylling, A., Mayer, B., Gasteiger, J., Hamann, U., Kylling, J., Richter, B., Pause, C., Dowling, T., and Bugliaro, L.: The libRadtran software package for radiative transfer calculations (version 2.0.1), Geosci. Model Dev., 9, 1647–1672, https://doi.org/10.5194/gmd-9-1647-2016, 2016.

Evans, K. F.: The spherical harmonics discrete ordinate method for three-dimensional atmospheric radiative transfer, J. Atmos. Sci., 55, 429–446, 1998.

Gatebe, C. K., Jethva, H., Gautam, R., Poudyal, R., and Várnai, T.: A new measurement approach for validating satellite-based above-cloud aerosol optical depth, Atmos. Meas. Tech., 14, 1405–1423, https://doi.org/10.5194/amt-14-1405-2021, 2021.

Gristey, J. J., Feingold, G., Glenn, I. B., Schmidt, K. S., and Chen, H.: Surface Solar Irradiance in Continental Shallow Cumulus Fields: Observations and Large-Eddy Simulation, J. Atmos. Sci., 77, 1065–1080, https://doi.org/10.1175/JAS-D-19-0261.1, 2020a.

Gristey, J. J., Feingold, G., Glenn, I. B., Schmidt, K. S., and Chen, H.: On the Relationship Between Shallow Cumulus Cloud Field Properties and Surface Solar Irradiance, Geophys. Res. Lett., 47, e2020GL090152, https://doi.org/10.1029/2020GL090152, 2020b.

Gristey, J. J., Feingold, G., Glenn, I. B., Schmidt, K. S., and Chen, H.: Influence of Aerosol Embedded in Shallow Cumulus Cloud Fields on the Surface Solar Irradiance, J. Geophys. Res.-Atmos., 127, e2022JD036822, https://doi.org/10.1029/2022JD036822, 2022.

Ham, S.-H., Kato, S., Barker, H. W., Rose, F. G., and Sun-Mack, S.: Improving the modelling of short-wave radiation through the use of a 3D scene construction algorithm, Q. J. Roy. Meteor. Soc., 141, 1870–1883, https://doi.org/10.1002/qj.2491, 2015.

Heidinger, A. K., Foster, M. J., Walther, A., and Zhao, X.: The Pathfinder Atmospheres-Extended AVHRR climate dataset, B. Am. Meteorol. Soc., 95, 909–922, https://doi.org/10.1175/BAMS-D-12-00246.1, 2014.

Illingworth, A. J., Barker, H. W., Beljaars, A., Chepfer, H., Delanoe, J., Domenech, C., Donovan, D. P., Fukuda, S., Hirakata, M., Hogan, R. J., Huenerbein, A., Kollias, P., Kubota, T., Nakajima, T., Nakajima, T. Y., Nishizawa, T., Ohno, Y., Okamoto, H., Oki, R., Sato, K., Satoh, M., Wandinger, U., Wehr, T., and van Zadelhoff, G.: The EarthCARE Satellite: the next step forward in global measurements of clouds, aerosols, precipitation and radiation, B. Am. Meteorol. Soc, 96, 1311–1332, https://doi.org/10.1175/BAMS-D-12-00227.1, 2015.

Iwabuchi, H.: Efficient Monte Carlo methods for radiative transfer modeling, J. Atmos. Sci., 63, 2324–2339, 2006.

Kindel, B. C., Schmidt, K. S., Pilewskie, P., Baum, B. A., Yang, P., and Platnick, S.: Observations and modeling of ice cloud shortwave spectral albedo during the Tropical Composition, Cloud and Climate Coupling Experiment (TC$^4$), J. Geophys. Res., 115, D00J18, https://doi.org/10.1029/2009JD013127, 2010.

King, M. and Platnick, S.: The Earth Observing System (EOS), Comprehensive Remote Sensing, 7, 7–26, https://doi.org/10.1016/b978-0-12-409548-9.10312-4, 2018.

Kurucz, R. L.: Synthetic infrared spectra, in: Proceedings of the 154th Symposium of the International Astronomical Union (IAU), Tucson, Arizona, 2–6 March 1992, Kluwer, Acad., Norwell, MA, 154, 523–531, https://doi.org/10.1017/S0074180900124805, 1992.

Levis, A., Schechner, Y. Y., Davis, A. B., and Loveridge, J.: Multi-View Polarimetric Scattering Cloud Tomography and Retrieval of Droplet Size, Remote Sens., 12, 2831, https://doi.org/10.3390/rs12172831, 2020.

Li, J., Scinocca, J., Lazare, M., McFarlane, N., von Salzen, K., and Solheim, L.: Ocean Surface Albedo and Its Impact on Radiation Balance in Climate Models, J. Climate, 19, 6314–6333, 2006.

Long, C. N., Bucholtz, A., Jonsson, H., Schmid, B., Vogelmann, A., and Wood, J.: A Method of Correcting for Tilt from Horizontal in Downwelling Shortwave Irradiance Measurements on Moving Platforms, Open Atmospheric Science Journal, 4, 78–87, 2010.

Loveridge, J., Levis, A., Di Girolamo, L., Holodovsky, V., Forster, L., Davis, A. B., and Schechner, Y. Y.: Retrieving 3D distributions of atmospheric particles using Atmospheric Tomography with 3D Radiative Transfer – Part 1: Model description and Jacobian calculation, Atmos. Meas. Tech. Discuss. [preprint], https://doi.org/10.5194/amt-2022-251, in review, 2022.

Marshak, A., Davis, A., Wiscombe, W., and Cahalan, R.: Radiative smoothing in fractal clouds, J. Geophys. Res., 100, 26247–26261, https://doi.org/10.1029/95JD02895, 1995.

Marshak, A., Wen, G., Coakley, J., Remer, L., Loeb, N. G., and Cahalan, R. F.: A simple model for the cloud adjacency effect and the apparent bluing of aerosols near clouds, J. Geophys. Res., 113, D14S17, https://doi.org/10.1029/2007JD009196, 2008.

Massie, S. T., Schmidt, K. S., Eldering, A., and Crisp, D.: Observational evidence of 3-D cloud effects in OCO-2 $CO_2$ retrievals, J. Geophys. Res.-Atmos., 122, 7064–7085, https://doi.org/10.1002/2016JD026111, 2017.

Masuda, R., Iwabuchi, H., Schmidt, K. S., Damiani, A. and Kudo, R.: Retrieval of Cloud Optical Thickness from Sky-View Camera Images using a Deep Convolutional Neural Network based on Three-Dimensional Radiative Transfer, Remote Sens., 11, 1962, https://doi.org/10.3390/rs11171962, 2019.

Mayer, B.: Radiative transfer in the cloudy atmosphere, EPJ Web Conf., 1, 75–99, https://doi.org/10.1140/epjconf/e2009-00912-1, 2009.

Mayer, B. and Kylling, A.: Technical note: The libRadtran software package for radiative transfer calculations – description and examples of use, Atmos. Chem. Phys., 5, 1855–1877, https://doi.org/10.5194/acp-5-1855-2005, 2005.

Mlawer, E. J., Taubman, S. J., Brown, P. D., Iacono, M. J., and Clough, S. A.: Radiative transfer for inhomogeneous atmospheres: RRTM, a validated correlated-k model for the longwave, J. Geophys. Res., 102, 16663–16682, 1997.

MODIS Characterization Support Team: MODIS Geolocation Fields Product, NASA MODIS Adaptive Processing System, Goddard Space Flight Center, USA [data set], https://doi.org/10.5067/MODIS/MYD03.061, 2017a.

MODIS Characterization Support Team: MODIS 250m Calibrated Radiances Product, NASA MODIS Adaptive Processing System, Goddard Space Flight Center, USA [data set], https://doi.org/10.5067/MODIS/MYD02QKM.061, 2017b.

Nakajima, T. and King, M. D.: Determination of the optical thickness and effective particle radius of clouds from reflected solar radiation measurements. Part I: Theory, J. Atmos. Sci., 47, 1878–1893, 1990.

Nataraja, V., Schmidt, S., Chen, H., Yamaguchi, T., Kazil, J., Feingold, G., Wolf, K., and Iwabuchi, H.: Segmentation-based multi-pixel cloud optical thickness retrieval using a convolutional neural network, Atmos. Meas. Tech., 15, 5181–5205, https://doi.org/10.5194/amt-15-5181-2022, 2022.

Norgren, M. S., Wood, J., Schmidt, K. S., van Diedenhoven, B., Stamnes, S. A., Ziemba, L. D., Crosbie, E. C., Shook, M. A., Kittelman, A. S., LeBlanc, S. E., Broccardo, S., Freitag, S., and Reid, J. S.: Above-aircraft cirrus cloud and aerosol optical depth from hyperspectral irradiances measured by a total-diffuse radiometer, Atmos. Meas. Tech., 15, 1373–1394, https://doi.org/10.5194/amt-15-1373-2022, 2022.

OCO-2 Science Team/Gunson, M., and Eldering, A.: OCO-2 Level 1B calibrated, geolocated science spectra, Retrospective Processing V10r, Greenbelt, MD, USA, Goddard Earth Sciences Data and Information Services Center (GES DISC) [data set], https://doi.org/10.5067/6O3GEUK7U2JG, 2019a.

OCO-2 Science Team/Gunson, M., and Eldering, A.: OCO-2 Level 2 meteorological parameters interpolated from global assimilation model for each sounding, Retrospective Processing V10r, Greenbelt, MD, USA, Goddard Earth Sciences Data and Information Services Center (GES DISC) [data set], https://doi.org/10.5067/OJZZW0LIGSDH, 2019b.

OCO-2 Science Team/Gunson, M., and Eldering, A.: OCO-2 Level 2 geolocated XCO2 retrievals results, physical model, Retrospective Processing V10r, Greenbelt, MD, USA, Goddard Earth Sciences Data and Information Services Center (GES DISC) [data set], https://doi.org/10.5067/6SBROTA57TFH, 2020.

O'Hirok, W. and Gautier, C.: The impact of model resolution on differences between independent column approximation and monte carlo estimates of shortwave surface irradiance and atmospheric heating rate, J. Atmos. Sci., 62, 2939–2951, https://doi.org/10.1175/jas3519.1, 2005.

Payne, V. H., Drouin, B. J., Oyafuso, F., Kuai, L., Fisher, B. M., Sung, K., Nemchicka, D., Crawford, T. J., Smyth, M., Crisp, D., Adkins, E., Hodges, J. T., Long, D. A., Mlawer, E. J., Merrelli, A., Lunny, E., and O'Dell, C. W.: Absorption coefficient (ABSCO) tables for the Orbiting Carbon Observatories: version 5.1, J. Quant. Spectrosc. Ra., 255, 1–16, https://doi.org/10.1016/j.jqsrt.2020.107217, 2020.

Pilewskie, P., Pommier, J., Bergstrom, R., Gore, W., Howard, S., Rabbette, M., Schmid, B., Hobbs, P. V., and Tsay, S. C.: Solar spectral radiative forcing during the Southern African Regional Science Initiative, J. Geophys. Res., 108, 8486, https://doi.org/10.1029/2002JD002411, 2003.

Pincus, R. and Evans, K. F.: Computational cost and accuracy in calculating three-dimensional radiative transfer: Results for new implementations of Monte Carlo and SHDOM, J. Atmos. Sci., 66, 3131–3146, 2009.

Platnick, S., King, M. D., Ackerman, S. A., Menzel, W. P., Baum, B. A., Rieìdi, J. C., and Frey, R. A.: The MODIS cloud products: Algorithms and examples from Terra, IEEE T. Geosci. Remote, 41, 459–473, 2003.

Platnick, S., Ackerman, S. A., King, M. D., Meyer, K., Menzel, W. P., Holz, R. E., Baum, B. A., and Yang, P.: MODIS atmosphere L2 cloud product (06_L2), NASA MODIS Adaptive Processing System, Goddard Space Flight Center, USA [data set], https://doi.org/10.5067/MODIS/MYD06_L2.061, 2015.

Reid, J. S., Xian, P., Burton, S. P., Cook, A. L., Crosbie, E. C., Fenn, M. A., Ferrare, R. A., Freeman, S. W., Hair, J. W., Harper, D. B., Hostetler, C. A., Robinson, C. E., Scarino, A. J., Shook, M. A., Sokolowsky, G. A., van den Heever, S. C., Winstead, E. L., Woods, S., and Ziemba, L. D.: Clouds, Aerosol and Monsoon Processes-Philippines Experiment, CAMP2Ex Data [data set], https://doi.org/10.5067/Suborbital/CAMP2EX2018/DATA001, 2022.

Reid, J. S., Maring, H. B., Narisma, G. T., van den Heever, S., Di Girolamo, L., Ferrare, R., Lawson, P., Mace, G. G., Simpas, J. B., Tanelli, S., Ziemba, L., van Diedenhoven, B., Bruintjes, R., Bucholtz, A., Cairns, B., Cambaliza, M. O., Chen, G., Diskin, G. S., Flynn, J. H., Hostetler, C. A., Holz, R. E., Lang, T. J., Schmidt, K. S., Smith, G., Sorooshian, A., Thompson, E. J., Thornhill, K. L., Trepte, C., Wang, J., Woods, S., Yoon, S., Alexandrov, M., Alvarez, S., Amiot, C. G., Bennett, J. R., Brooks, M., Burton, S. P., Cayanan, E., Chen, H., Collow, A., Crosbie, E., DaSilva, A., DiGangi, J. P., Flagg, D. D., Freeman, S. W., Fu, D., Fukada, E., Hilario, M. R. A., Hong, Y., Hristova-Veleva, S. M., Kuehn, R., Kowch, R. S., Leung, G. R., Loveridge, J., Meyer, K., Miller, R. M., Montes, M. J., Moum, J. N., Nenes, T., Nesbitt, S. W., Norgren, M., Nowottnick, E. P., Rauber, R. M., Reid, E. A., Rutledge, S., Schlosser, J. S., Sekiyama, T. T., Shook, M. A., Sokolowsky, G. A., Stamnes, S. A., Tanaka, T. Y., Wasilewski, A., Xian, P., Xiao, Q., Xu, Z., and Zavaleta, J.: The coupling between tropical meteorology, aerosol lifecycle, convection, and radiation, during the Clouds, Aerosol and Monsoon Processes Philippines Experiment (CAMP$^2$Ex), B. Am. Meteorol. Soc., https://doi.org/10.1175/BAMS-D-21-0285.1, in press, 2023.

Ronneberger, O., Fischer, P., and Brox, T.: U-net: Convolutional networks for biomedical image segmentation, in: International Conference on Medical image computing and computer-assisted intervention, Springer, 234–241, https://doi.org/10.1007/978-3-319-24574-4_28, 2015.

Rothman, L., Jacquemart, D., Barbe, A., Chris Benner, D., Birk, M., Brown, L., Carleer, M., Chackerian, C., Chance, K., Coudert, L., Dana, V., Devi, V., Flaud, J.-M., Gamache, R., Goldman, A., Hartmann, J.-M., Jucks, K., Maki, A., Mandin, J.-Y., Massie, S., Orphal, J., Perrin, A., Rinsland, C., Smith, M., Tennyson, J., Tolchenov, R., Toth, R., Vander Auwera, J., Varanasi, P., and Wagner, G.: The HITRAN 2004 molecular spectroscopic database, J. Quant. Spectrosc. Ra., 96, 139–204, https://doi.org/10.1016/j.jqsrt.2004.10.008, 2005.

Schaaf, C. and Wang, Z.: MODIS/Terra+Aqua BRDF/Albedo Daily L3 Global – 500m V061, NASA EOSDIS Land Processes DAAC [data set], https://doi.org/10.5067/MODIS/MCD43A3.061, 2021.

Schmidt, K. S., Pilewskie, P., Platnick, S., Wind, G., Yang, P., and Wendisch, M.: Comparing irradiance fields derived from Moderate Resolution Imaging Spectroradiometer airborne simulator cirrus cloud retrievals with solar spectral flux radiometer measurements, J. Geophys. Res., 112, D24206, https://doi.org/10.1029/2007JD008711, 2007.

Schmidt, S., Pilewskie, P., Mayer, B., Wendisch, M., Kindel, B., Platnick, S., King, M. D., Wind, G., Arnold, G. T., Tian, L., Heymsfield, G., and Kalesse, H.: Apparent absorption of solar spectral irradiance in heterogeneous ice clouds, J. Geophys. Res., 115, D00J22, https://doi.org/10.1029/2009JD013124, 2010.

Song, S., Schmidt, K. S., Pilewskie, P., King, M. D., Heidinger, A. K., Walther, A., Iwabuchi, H., Wind, G., and Coddington, O. M.: The spectral signature of cloud spatial structure in shortwave irradiance, Atmos. Chem. Phys., 16, 13791–13806, https://doi.org/10.5194/acp-16-13791-2016, 2016.

Spada, F., Krol, M. C., and Stammes, P.: McSCIA: application of the Equivalence Theorem in a Monte Carlo radiative transfer model for spherical shell atmospheres, Atmos. Chem. Phys., 6, 4823–4842, https://doi.org/10.5194/acp-6-4823-2006, 2006.

Strahler, A., Muller, J., Lucht, W., Schaaf, C., Tsang, T., Gao, F., Li, X., Lewis, P., and Barnsley, M.: MODIS BRDF/albedo product: algorithm theoretical basis document version 5.0, MODIS documentation, https://modis.gsfc.nasa.gov/data/atbd/atbd_mod09.pdf (last access: 6 April 2023), 1999.

Várnai, T., Marshak, A., and Huang, C.-H.: Publicly available online simulator of 3D radiative processes, International Radiation Symposium 2022, Thessaloniki, Greece, 4–8 July 2022, https://mycloud.auth.gr/index.php/s/t7fYkzsiFWYFdqy?dir=undefined&path=%2FS4-General_Remote_Sensing&openfile=2669790 (last access: 6 April 2023), 2022.

Wood, J., Smyth, T. J., and Estellés, V.: Autonomous marine hyperspectral radiometers for determining solar irradiances and aerosol optical properties, Atmos. Meas. Tech., 10, 1723–1737, https://doi.org/10.5194/amt-10-1723-2017, 2017.